Journal of Applied Physics

RESEARCH ARTICLE | MAY 08 2024

Impacts of vacancy complexes on the room-temperature photoluminescence lifetimes of state-of-the-art GaN substrates, epitaxial layers, and Mg-implanted layers

Shigefusa F. Chichibu ; Kohei Shima ; Akira Uedono ; Shoji Ishibashi ; Hiroko Iguchi ; Tetsuo Narita ; Keita Kataoka ; Ryo Tanaka ; Shinya Takashima ; Katsunori Ueno; Masaharu Edo; Hirotaka Watanabe; Atsushi Tanaka; Yoshio Honda ; Jun Suda ; Hiroshi Amano ; Tetsu Kachi ; Toshihide Nabatame ; Yoshihiro Irokawa ; Yasuo Koide

J. Appl. Phys. 135, 185701 (2024)
https://doi.org/10.1063/5.0201931

AIP Publishing

Journal of Applied Physics ARTICLE pubs.aip.org/aip/jap

Impacts of vacancy complexes on the room-temperature photoluminescence lifetimes of state-of-the-art GaN substrates, epitaxial layers, and Mg-implanted layers

Cite as: J. Appl. Phys. **135**, 185701 (2024); doi: 10.1063/5.0201931
Submitted: 1 February 2024 · Accepted: 19 April 2024 ·
Published Online: 8 May 2024

Shigefusa F. Chichibu,[1,a)] Kohei Shima,[1] Akira Uedono,[2] Shoji Ishibashi,[3] Hiroko Iguchi,[4] Tetsuo Narita,[4] Keita Kataoka,[4] Ryo Tanaka,[5] Shinya Takashima,[5] Katsunori Ueno,[5] Masaharu Edo,[5] Hirotaka Watanabe,[6] Atsushi Tanaka,[6] Yoshio Honda,[6] Jun Suda,[6] Hiroshi Amano,[6] Tetsu Kachi,[6] Toshihide Nabatame,[7] Yoshihiro Irokawa,[7] and Yasuo Koide[7]

AFFILIATIONS

[1]Institute of Multidisciplinary Research for Advanced Materials, Tohoku University, Sendai 980-8577, Japan
[2]Division of Applied Physics, Faculty of Pure and Applied Science, University of Tsukuba, Tsukuba 305-8573, Japan
[3]Research Center for Computational Design of Advanced Functional Materials, National Institute of Advanced Industrial Science and Technology, Tsukuba 305-8568, Japan
[4]Toyota Central R&D Labs., Inc., Nagakute, Aichi 490-1192, Japan
[5]Advanced Technology Laboratory, Fuji Electric Co., Ltd., Hino, Tokyo 191-8502, Japan
[6]Institute of Materials and Systems for Sustainability, Nagoya University, Nagoya 464-8601, Japan
[7]National Institute for Materials Science, Tsukuba 305-0047, Japan

Note: This paper is part of the special topic, Native Defects, Impurities and the Electronic Structure of Compound Semiconductors: A Tribute to Dr. Wladyslaw Walukiewicz.

[a)]**Author to whom correspondence should be addressed:** chichibulab@yahoo.co.jp

ABSTRACT

For rooting the development of GaN-based optoelectronic devices, understanding the roles of midgap recombination centers (MGRCs), namely, nonradiative recombination centers and deep-state radiative recombination centers, on the carrier recombination dynamics is an essential task. By using the combination of time-resolved photoluminescence and positron annihilation spectroscopy (PAS) measurements, the origins of major MGRCs in the state-of-the-art GaN epilayers, bulk crystals, and Mg-implanted layers were identified, and their concentrations were quantified for deriving the capture coefficients of minority carriers. In this article, potential standardization of the room-temperature photoluminescence lifetime for the near-band-edge emission (τ_{PL}^{RT}) as the concentration of major MGRCs well below the detection limit of PAS is proposed. For n-GaN substrates and epilayers grown from the vapor phase, τ_{PL}^{RT} was limited by the concentration of carbon on N sites or divacancies comprising a Ga vacancy (V_{Ga}) and a N vacancy (V_N), [$V_{Ga}V_N$], when carbon concentration was higher or lower, respectively, than approximately 10^{16} cm^{-3}. Here, carbon and $V_{Ga}V_N$ act as major deep-state radiative and nonradiative recombination centers, respectively, while major MGRCs in bulk GaN crystals were identified as $V_{Ga}(V_N)_3$ vacancy clusters in Na-flux GaN and V_{Ga} or $V_{Ga}V_N$ buried by a hydrogen and/or V_{Ga} decorated with oxygen on N sites, $V_{Ga}(O_N)_{3-4}$, in ammonothermal GaN. The values of τ_{PL}^{RT} in n-GaN samples are compared with those of p-GaN, in which τ_{PL}^{RT} was limited by the concentration of $V_{Ga}(V_N)_2$ in Mg-doped epilayers and by the concentrations of $V_{Ga}V_N$ and $(V_{Ga}V_N)_3$ in Mg-implanted GaN right after the implantation and after appropriate activation annealing, respectively.

I. INTRODUCTION

For bridging the sustainable development goals, the exploitation of energy-saving, high-power electronic devices[1] and advanced solid-state lighting[2] based on high-efficiency light-emitting diodes (LEDs)[3] is one of the significant ways. Gallium nitride (GaN) and related (Al,Ga,In)N alloys are a suitable candidate for such a purpose: InGaN alloys are used in near ultraviolet (UV) to visible LEDs and laser diodes (LDs) as well as in white LEDs comprising an InGaN quantum well (QW) blue LED and yellow phosphors.[3] It is quite important to note that such consumer LEDs are grown on heteroepitaxial GaN or AlN films on a *c*-plane Al_2O_3 substrate, generally labeled "GaN template" or "AlN template," respectively. Because both GaN and AlN have large lattice mismatch ($\Delta a/a > 16\%$) against Al_2O_3, the entire LED structure contains high-density threading dislocations (TDs) in the order of 10^8–$10^{10}\,cm^{-2}$. Nevertheless, such high threading dislocation density (TDD) InGaN QWs exhibit sufficiently high-intensity near-band-edge (NBE) emissions with the aid of defect- and polarization field-tolerant[2,4–6] radiation probability of localized excitons.[4] GaN also has a potential to achieve high-power transistors workable at high frequencies,[1] relying on its outstanding characteristics including the large bandgap energy (E_g) of 3.4 eV, high break-down field strength of 3.3 MV/cm,[7] and high saturation electron velocity of $2.5 \times 10^7\,cm\,s^{-1}$ (Ref. 8). A normally-off vertical GaN-based transistor on a GaN substrate exhibiting a low specific on-state resistance (R_{ON}) of $1\,m\Omega\,cm^2$ and a high off-state breakdown voltage (V_{BD}) of 1.7 kV has been demonstrated by fabricating a p-type GaN (p-GaN)/unintentionally doped (UID) AlGaN/GaN heterostructure.[9] Moreover, vertically current flowing GaN metal–oxide–semiconductor field-effect-transistors capable of large current switching have been explored progressively.[10–12] However, further improvements in the device performances, for example, better stability and reliability, are preferred to integrate GaN power devices in consumer systems.

For rooting the realization of such high-performance GaN-based devices, the use of large-area, single-domain, mosaic- and bowing-free GaN wafers of low TDD is preferred. As for GaN power devices,[1,9] highly pure designated electron concentration n^--type drift layer, p-GaN layer or p-GaN segments fabricated by selective area Mg ion implantation (I/I) for inversion channels, and high carrier concentration n^+ and p^+ contacting layers are indispensable. While, low optical absorption waveguiding and cladding layers as well as quantum-structured active regions hardly affected by midgap recombination (MGR) channels that shorten carrier lifetimes are required. There are a variety of MGR channels such as structural defects like cracks; voids; grain boundaries; stacking faults (SFs); TDs with edge, screw, and mixed components; surface defects causing surface recombinations; and bulk deep levels (DLs) originating from impurities and/or point defects. With respect to (Al,In,Ga)N, TDs higher than $10^8\,cm^{-2}$ had been invoked to as the dominant nonradiative recombination (NR) channels that limit the internal quantum efficiency (η_{int}) of the NBE emission (η_{int}^{NBE}).[13] With the aid of the appearance of freestanding (FS) GaN or AlN substrates, typical TDDs in (Al,Ga,In)N films have been decreased to below $10^7\,cm^{-2}$ and the corresponding TD spacings ($>3\,\mu m$) have become much longer than the diffusion length (L_D) of minority carriers ($L_{minority}$): in most cases, holes (L_p) in (Al,Ga,In)N. However, η_{int}^{NBE} has not reached unity.[14] Therefore, η_{int}^{NBE} of state-of-the-art (Al,Ga,In)N LEDs is no longer limited by TDs but limited by other MGR channels, most likely intrinsic point

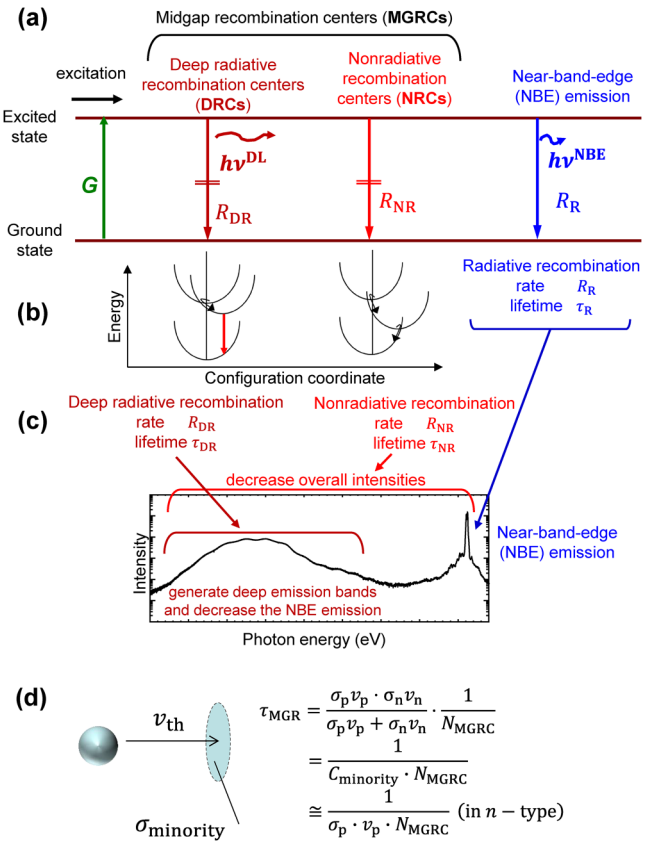

FIG. 1. Schematic representation of (a) the relationship among the excitation of e–h pairs or excitons with the rate *G*, radiative recombination emitting the NBE luminescence with the rate R_R (lifetime τ_R), nonradiative recombination at NRCs with the rate R_{NR} (lifetime τ_{NR}), and deep radiative recombination emitting the DL luminescence band with the photon energy $h\nu^{DL}$ at DRCs with rate R_{DR} (lifetime τ_{DR}). The model is drawn for the case of weak-excitation conditions to underline the midgap recombination (MGR) processes with negligible classical[17,18] and trap-assisted[19] Auger–Meitner nonradiative recombination (NR) processes. Both NRCs and DRCs obey the Shockley–Read–Hall (SRH) statistics[20,21] emitting only phonons and photons with the energy $h\nu^{DL}$ in addition to phonons, respectively, as shown using the configuration coordinate model in panel (b), and accordingly, they are categorized as MGRCs. (c) The roles of the three types of recombinations on the luminescence spectrum. Radiative recombination generates the NBE emission, nonradiative recombination decreases overall luminescence intensity, and deep radiative recombination emits a DL luminescence band and decreases the NBE emission intensity. (d) Schematic model of MGRCs in an n-type semiconductor that capture minority carriers (holes) with the capture coefficient C_p, which is a product of capture cross section σ_p and thermal velocity v_{th} (v_p). According to the SRH statistics,[20,21] MGR lifetime (τ_{MGR}) is expressed by Eqs. (2) and (3), namely, $\tau_{MGR} = \frac{1}{C_{minority} \times N_{MGRC}} \cong \frac{1}{\sigma_p \times v_p \times N_{MGRC}}$, where $C_{minority} = C_p = \sigma_p \times v_p$ is a hole capture coefficient [Modified with permission from Chichibu *et al.*, J. Appl. Phys. **123**, 161413 (2018). Copyright 2018 AIP Publishing LLC].[25]

defects,[15] impurities, or their complexes. Consequently, origins and properties of MGR channels in GaN are worth investigating. Such recombination centers are expressed "midgap recombination centers (MGRCs)" in this article.

The essence of the roles of MGRCs on the carrier recombination phenomena is summarized[16] in Fig. 1: MGRCs cause carrier recombination emitting only phonons or phonons plus photons with energy ($h\upsilon$) defined as $h\upsilon^{DL}$, which is lower than E_g. The MGRCs with and without $h\upsilon^{DL}$ emission are classified into "deep-state radiative recombination centers (DRCs)" and "nonradiative recombination centers (NRCs)," respectively. In Fig. 1(b), the configuration coordinate model is used to show Stokes' shifts for a DL luminescence by DRCs. After the excitation of electron–hole (e–h) pairs or excitons with the rate G, the exited quanta recombine through (i) a direct radiative recombination emitting the NBE luminescence such as free exciton (FX) emission, bound exciton (BX) emission, and band-to-band emission with a representative rate R_R (lifetime τ_R), (ii) NR recombination at NRCs with a rate R_{NR} (lifetime τ_{NR}), and (iii) sequential NR and radiative recombinations emitting $h\upsilon^{DL}$ at DRCs with the rate R_{DR} (lifetime τ_{DR}). We should mention that Fig. 1 is drawn for the case of weak-excitation conditions to underline the MGR processes. Here, the definition of "weak-excitation conditions" throughout this paper is that the excited carrier or exciton concentration ($n_{excited}$) is far less than the majority carrier concentration giving rise to $n_{excited}$ as minority carrier concentration and also far below the threshold for maintaining negligible classical[17,18] and trap-assisted[19] Auger–Meitner nonradiative recombination processes. According to the Shockley–Read–Hall (SRH) statistics[20,21] represented in Fig. 1(d), overall MGR lifetime (τ_{MGR}), which is an inverse of the rate R_{MGR} and is a function of τ_{NR} and τ_{DR},

$$\frac{1}{\tau_{MGR}} = \frac{1}{\tau_{NR}} + \frac{1}{\tau_{DR}}, \tag{1}$$

is expressed by

$$\tau_{MGR} = \frac{\sigma_p \nu_p \times \sigma_n \nu_n}{\sigma_p \nu_p + \sigma_n \nu_n} \cdot \frac{1}{N_{MGRC}}, \tag{2}$$

where N_{MGRC} is the concentration of MGRCs; σ_p and σ_n are the capture cross sections and ν_p and ν_n are thermal velocities for a hole and an electron, respectively. In n-GaN, Eq. (2) is approximated by

$$\tau_{MGR} \cong \frac{1}{C_{minority} \times N_{MGRC}} = \frac{1}{\sigma_p \times \nu_p \times N_{MGRC}}, \tag{3}$$

where $C_p = C_{minority}$, $\sigma_p = \sigma_{minority}$, and $\nu_p = \nu_{minority}$ are the capture coefficient, capture cross section, and thermal velocity (ν_{th}), respectively, for a minority carrier (hole). Here, $\nu_p = \nu_{th} = \sqrt{\frac{3k_BT}{m_p}}$, where k_B is the Boltzmann constant, T is the temperature, and m_p is the hole effective mass.

Generally, MGRCs play an important role in limiting η_{int}^{NBE}, which is expressed by

$$\eta_{int}^{NBE} = \frac{R_R}{(R_R + R_{NR} + R_{DR})} = \frac{\frac{1}{\tau_R}}{\left(\frac{1}{\tau_R} + \frac{1}{\tau_{NR}} + \frac{1}{\tau_{DR}}\right)} = \frac{1}{1 + \frac{\tau_R}{\tau_{MGR}}}. \tag{4}$$

Because τ_R in the bulk semiconductor is unique to a material under fixed carrier concentration at a given temperature (T), τ_{MGR} limits η_{int}^{NBE}. With increasing T, τ_{MGR} is supposed to first decrease due to the increase in ν_{th} and reach a constant value[22,23] when L_D of a minority carrier $\left(L_{minority} = \sqrt{D_{minority} \times \tau_{minority}}\right)$ reaches approximately half of the average MGRC spacing, where $D_{minority}\left(= \frac{k_BT}{q} \times \mu_{minority}\right)$ and $\tau_{minority}$ are the diffusivity and lifetime of a minority carrier, respectively, where $\mu_{minority}$ is a minority carrier mobility. Accordingly, N_{MGRC} limits $\tau_{minority}$ of low- to medium- (or even high-) grade GaN at room temperature. Here, $\tau_{minority}$ can be quantified as a photoluminescence (PL) lifetime (τ_{PL}) in (Al,Ga,In)N under weak-excitation conditions defined in the preceding paragraph,[22,24–28]

$$\frac{1}{\tau_{PL}} = \frac{1}{\tau_{minority}} = \frac{1}{\tau_R} + \frac{1}{\tau_{MGR}}. \tag{5}$$

Here, we note again that other important NR recombination processes are classical[17,18] and trap-assisted[19] Auger–Meitner recombinations, which arise from different mechanisms and become significant under medium- to high-excitation conditions. According to Eq. (5), room-temperature PL lifetime for the NBE emission (τ_{PL}^{RT}) of GaN under the weak-excitation conditions[22,24–28] can be predicted as a function of N_{MGRC} and $C_{minority}$ using the room-temperature τ_R value (τ_R^{RT}) of approximately 40 ns for GaN (Refs. 22 and 23), as shown in Fig. 9 of Ref. 25, in which corresponding η_{int}^{NBE} has been calibrated on the right vertical axis. We note that typical $C_{minority}$ of MGRCs reported for n-GaN, p-GaN, and Mg ion-implanted (I/I) GaN are in the range between 10^{-8} and 10^{-5} cm^3 s^{-1}, as described later.[25–32] For high N_{MGRC} regime, τ_{PL}^{RT} linearly decreases with increasing N_{MGRC}.

For decreasing N_{MGRC}, in-depth probing of $\tau_{minority}$ and knowing true origins of MGRCs are essential tasks. For this mission, a combinatorial use[24–28] of positron annihilation spectroscopy (PAS)[33–38] and time-resolved photoluminescence (TRPL) measurements is advantageous because PAS identifies the species[37–41] and quantifies the concentration[25–28,42–44] of vacancy-type defects while TRPL quantifies[22–30] τ_{PL}, which represents $\tau_{minority}$ under weak-excitation conditions.[22,24–28] By using this combinatorial approach, some of the authors have long been suggesting since 2005 (Ref. 24) that vacancy complexes[22,24] comprising a Ga vacancy (V_{Ga}), more precisely divacancies comprising a V_{Ga} and a nitrogen vacancy (V_N), namely, $V_{Ga}V_N$, are the origin of predominant intrinsic NRCs in a variety of UID and n-type GaN;[25] the details will be explained in Sec. II. We should note that in 1990s, several theorists have predicted the presence of V_{Ga} and V_N in GaN, and the importance of V_{Ga} on the "yellow luminescence (YL)" band[45–47] at around 2.2 eV and the NR recombination[48,49]

has been proposed. However, experimental evidence showing the presence of V_{Ga} has not been reported[48,49] until 1997 when Saarinen *et al.*[35] have probed V_{Ga} in GaN by using PAS technique. Uedono *et al.*[36] have supported the existence of V_{Ga} in GaN epilayers using PAS later in 2001. Nevertheless, our assignment[24,25] is basically consistent with the results of the calculations[46,50,51] that the formation energy (E_{Form}) of negatively charged defects such as V_{Ga}^{-} in GaN can become lower due to the Fermi level (E_F) term ($+qE_F$).[46,50,51]

In this article, the origins and $C_{minority}(\sigma_{minority})$ of major MGRCs in the state-of-the-art GaN epilayers, bulk crystals, and Mg-I/I layers obtained by using the combinatorial PAS and TRPL measurements are summarized to propose a potential standardization of the weak excitation[22,24–28] τ_{PL}^{RT} as the concentration of major MGRCs well below the detection limit of PAS measurement. As for UID and n-type GaN substrates and epilayers grown by halide vapor phase epitaxy (HVPE) and metalorganic vapor phase epitaxy (MOVPE), τ_{PL}^{RT} was limited by the concentration of carbon impurities substituted on N sites ($[C_N]$) when $[C_N]$ was higher than approximately $10^{16}\,cm^{-3}$: $C_N^{0/-}$ is the origin of the YL band.[47] τ_{PL}^{RT} was limited by the concentration of $V_{Ga}V_N$ ($[V_{Ga}V_N]$) that act as major NRCs when $[C_N]$ was lower than approximately $10^{16}\,cm^{-3}$. The GaN crystals grown by the Na-flux method contained larger-size $V_{Ga}(V_N)_3$ vacancy clusters while those grown by the ammonothermal (AT) method contained vacancy complexes such as V_{Ga} or $V_{Ga}V_N$ buried by a hydrogen (H_{Ga} and $H_{V_{Ga}V_N}$, respectively) and/or V_{Ga} decorated with oxygen (O) impurities on N sites, $V_{Ga}(O_N)_{3–4}$, and all these vacancy complexes appear to act as MGRCs. For Mg-doped p-type GaN epilayers, τ_{PL}^{RT} was limited by the concentration of $V_{Ga}(V_N)_2$, $[V_{Ga}(V_N)_2]$. For Mg-I/I GaN, $V_{Ga}V_N$ and $(V_{Ga}V_N)_3$ are the major NRCs right after the implantation and after appropriate post-implantation annealings (PIAs), respectively. Because of larger σ_n of $V_{Ga}(V_N)_2$ and $(V_{Ga}V_N)_3$ and faster v_n, τ_{PL}^{RT} of p-GaN becomes approximately an order of magnitude shorter than that of n-GaN with the same N_{MGRC}.

II. EXPERIMENTAL AND ANALYTICAL DETAILS

For elucidating the species, concentration, and $C_{minority}$ of vacancy-type defects in GaN, various crystals and epilayers grown by a variety of methods and thin layers prepared by Mg-I/I technique were analyzed. At first, PAS measurement[33–38] and theoretical calculations[38–44] were carried out to identify the species and quantify the concentrations of major vacancy-type defects. The samples were also inspected by impurity analyses using secondary-ion mass spectrometry (SIMS) measurement. Then, TRPL measurement was carried out to quantify $\tau_{PL}^{RT}(=\tau_{MGR})$. When τ_{MGR} was inversely proportional to the concentration of a unique defect (N_{MGRC}), the defect could be assigned as the major MGRCs. Then, $C_{minority} = \sigma_{minority} \times v_{minority}$ of the MGRCs can be derived using Eq. (3).

A. Samples

Specifications of UID or doped n-GaN samples are summarized in Table I. The data in column "General information" are merely typical ones and N.A. indicates "not available." Supplier identifications (IDs) are represented by bold italic capital letters. Suppliers ***A***, ***B***, ***C***, and ***D*** grew "thick" GaN layers by HVPE under the growth conditions listed on the table. These samples included both *c*-plane and *m*-plane epilayers and FS-GaN substrates; the latter were fabricated by slicing thick GaN boule detached from foreign substrates. These samples were bowed mosaic crystals but had flat surface by appropriate polishing treatments. They contained low concentration of carbon ([C]), as the Ga precursor (GaCl) nor NH_3 contain C in the molecule. Suppliers ***E***, ***F***, and ***G*** grew a few-μm-thick GaN layers by MOVPE under the growth conditions listed on the table. These samples also included *c*-plane and *m*-plane epilayers. For MOVPE samples, it was difficult to decrease [C] less than $3\times10^{15}\,cm^{-3}$ due to the incorporation of C from the metalorganic Ga precursors such as trimethylgallium (TMGa). The [C] values were close to those reported previously by several other researchers:[52–55] [C] and some other impurity concentrations were quantified by the SIMS measurement. In HVPE and MOVPE GaN samples (***A***–***G***), [C] was varied from low ($1\times10^{15}\,cm^{-3}$) to high ($\sim10^{17}\,cm^{-3}$) concentrations, and typical TDD were less than a few times $10^6\,cm^{-2}$.

Bulk crystals of GaN were grown from the liquid phase or in the supercritical state. Suppliers ***H*** and ***J*** grew GaN crystals by the Na-flux method[56] using Na–Ga melt[57] or Na vapor,[58,59] respectively. Details of the growths other than the growth temperature (T_g) or growth pressure (P_g) have been given in Refs. 57–59. Supplier ***K*** grew Ge-doped ($3\times10^{18}\,cm^{-3}$) GaN by using the liquid-phase epitaxy (LPE) method, of which [C] was quantified to be $3\times10^{17}\,cm^{-3}$ by SIMS measurement. The growth details are undisclosed, although TDD was less than $5\times10^6\,cm^{-2}$. Suppliers ***L*** and ***M*** grew GaN crystals by the AT methods using basic mineralizers within the supercritical ammonia, namely, basic ammonothermal (BAT) methods, at high-pressure conditions (>200 MPa). On another front, suppliers ***N*** and ***P*** grew GaN crystals by the AT methods using acidic mineralizers within the supercritical ammonia, namely, acidic ammonothermal (AAT) methods. The growths were carried out at P_g up to 300 MPa (Ref. 60) for supplier ***N*** and approximately 100 MPa (Ref. 61) for supplier ***P***. Because P_g for ***P*** is much lower than that for ***N***, the method of supplier ***P*** has been named the low-pressure acidic ammonothermal (LPAAT) method,[61] which is forecasted to provide large-size bulk GaN crystals with the aid of the thinner wall thickness of the autoclave of the same outer diameter. In the case of AAT methods, a corrosion-resistant lining was carried out using noble metals on the inner wall of the autoclave made of Ni-based superalloys. Conversely, such noble metal lining cannot be applied in BAT autoclaves because the ammonobasic fluids corrode such noble metals. Accordingly, the incorporation of metals from a corroded autoclave is inescapable in BAT growths of GaN.

Specifications of Mg-doped p-type GaN samples are summarized in Table II. The data in the column "General information" are again merely typical ones. Suppliers ***Q*** and ***R***, which are suppliers A and B in Ref. 26, respectively, grew a few-μm-thick Mg-doped p-GaN layer by MOVPE on GaN substrates prepared by HVPE. The Mg concentration, [Mg], was varied from 3×10^{16} to $7\times10^{19}\,cm^{-3}$ (Refs. 26 and 42). Suppliers ***S***, ***T***, and ***U*** prepared Mg-I/I layers using GaN substrates or MOVPE GaN films on GaN substrates, in order to minimize potential influences of TDs on the luminescent properties. All Mg-I/I layers essentially had a box-shaped Mg profile fabricated using multistage I/I with different

TABLE I. Specifications of unintentionally doped (UID) or doped n-type GaN samples. The data in the column "General information" are merely typical ones and N.A. indicates "not available."

Supplier ID	Growth method		Typical conditions		General information	
	States	Method	Temperature (T_g) (°C)	Pressure (P_g) (MPa)	Point defect species	Fast component of the room-temperature PL lifetime (τ_{PL}^{RT}) (ns)
A	Vapor	Halide vapor phase epitaxy (HVPE)	1000–1150	0.001–0.1	$V_{Ga}V_N$[a]	0.4 to a few
B						0.2–0.7
C						0.2 to a few
D						0.02–0.1
E		Metalorganic vapor phase epitaxy (MOVPE)	1000–1100	0.01–0.1		0.31–0.34
F						0.2–0.6
G						0.1–0.6
H	Liquid	Na flux (melt)	800–900	4–10	$V_{Ga}(V_N)_3$[b]	N.A.
J		Na flux (vapor)[c,d]			N.A.	0.05–0.23[d]
K		Liquid phase epitaxy (LPE)	Undisclosed but Ge doped (3×10^{18} cm^{-3})		N.A.	0.035
L	Supercritical	Basic ammonothermal (BAT)	500–600	200–450	$V_{Ga}(O_N)_4$	<0.004
M						<0.001
N		Acidic ammonothermal (AAT)	500–600	~200[e]	$H_{V_{Ga}V_N}$ or	0.003[g]
P			500–630	~100[f]	$V_{Ga}(O_N)_4$[e]	0.040[g]

[a]Identified in Ref. 25.
[b]Identified in Ref. 57.
[c]Ref. 58.
[d]Measured in Ref. 59.
[e]Ref. 60.
[f]Ref. 61.
[g]Ref. 94.

TABLE II. Specifications of Mg-doped p-type GaN samples. The data in the column "General information" are merely typical ones. N.A. indicates "not available."

	Preparation method		Typical conditions		General information	
Supplier ID	Category	Method	Growth or annealing temperature (°C)	Growth or annealing pressure (MPa)	Point defect species	Room-temperature PL lifetime (τ_{PL}^{RT}) (ns)
Q	Epitaxy	Metalorganic vapor phase epitaxy (MOVPE)	$T_g \sim 1000$	$P_g = 0.001–0.1$	$V_{Ga}(V_N)_2$[a]	<0.001–0.025[b]
R						0.002–0.080[b]
S	Ion implantation (I/I)	Mg and H sequential I/I on N-polar GaN[c,d]	$T_a = 800–1260$	$P_a = 0.1$	$(V_{Ga}V_N)_3$[d]	0.003–0.018[c]
T		Mg and N sequential I/I on Ga-polar GaN (vacancy-guided)[e,f]	$T_a = 1000–1300$	$P_a = 0.1$	$(V_{Ga}V_N)_3$[e]	0.0014[f]
U		Mg I/I without capping[g]	$T_a = 1000–1480$	$P_a = 1000$[h]	$(V_{Ga}V_N)_3$[i]	<0.001[j]

[a]Ref. 42.
[b]Ref. 26.
[c]Ref. 27.
[d]Ref. 43.
[e]Ref. 62.
[f]Ref. 63.
[g]Ref. 64.
[h]Ref. 65.
[i]Ref. 44.
[j]Ref. 99.

acceleration energies from 20 to 420 keV with different doses at room temperature.[27,28,42–44,62–64] The samples provided by supplier ***S*** were sequentially Mg- and H-implanted N-polar GaN substrates (I/I-GaN:Mg + H).[27,43] For comparison, the same I/Is were carried out on a Ga-polar MOVPE epilayer.[27] The samples provided by the supplier ***T*** were sequentially Mg- and N-implanted Ga-polar MOVPE epilayers.[62,63] For these samples, very shallow implantation of Mg was followed by the box-shaped deep implantation of N, in order to give rise to the "vacancy-guided redistribution (VGR)"[62,63] of Mg and to decrease the concentration of V_N, $[V_N]$, by burying V_N with the "excess" implanted N. Indeed, gross I/I damage for the VGR technique was lower than the conventional multistage I/I of Mg. Supplier ***U*** carried out so-called "ultrahigh-pressure annealing (UHPA)"[64,65] of Mg-I/I GaN on GaN up to 1480 °C at 1 GPa in N_2. The most remarkable advantage of using UHPA[64,65] is that high-pressure N_2 suppresses surface decomposition of GaN during high-temperature annealing up to 1480 °C, without any capping layers on the implanted surface. Accordingly, surface damages due to the thermal stress are prevented and p-GaN layers of excellent electrical properties are routinely obtained.[64]

B. Positron annihilation spectroscopy

Positron annihilation spectroscopy (PAS)[33–38] is an established, nondestructive, and exclusive tool for detecting neutral and negatively charged vacancy-type defects in a semiconductor. A positron (e^+) is an antimatter of an electron (e^-) having a positive charge with a mass (m) identical to that of e^-. Implanted e^+ annihilates with a surrounding e^- and emits two γ rays. According to the relationship $E_\gamma = mc^2$, E_γ is approximately 511 keV, where E_γ is the energy of the γ ray and c is the speed of the light. The annihilating γ-ray spectra are broadened in energy due to the momentum distribution of the annihilating electron–positron ($e^- - e^+$) pair p_L, which is parallel to the direction of the γ rays. The energy of the γ rays is expressed as $E_\gamma = mc^2 \pm \Delta E_\gamma$. The Doppler shift ΔE_γ is given by the relationship $\Delta E_\gamma = p_L c/2$.

A freely diffusing e^+ likely localizes in a vacancy-type defect because of Coulomb repulsion from ion cores. Because the momentum distribution of e^- surrounding vacancy-type defects is smaller than that in defect-free (DF) delocalized regions due to larger contribution of valence electrons, the defects can be detected by measuring the Doppler broadening spectra of the γ rays. The resulting change in the γ-ray spectra is characterized by the line shape parameter S and the wing parameter W, where the former mainly reflects the fraction of annihilating $e^- - e^+$ pairs of small momentum distribution (mostly valence electrons) and the latter represents the fraction of the pairs of large momentum distribution (mostly core electrons). Since V_{Ga} and vacancy complexes comprising V_{Ga} may form acceptor-type defects in GaN, they are the most probable candidates of e^+ trapping centers.[35–38] Accordingly, (S, W) coordinates can be used as a measure of species and concentration of V_{Ga} and vacancy complexes comprising V_{Ga}.

In order to identify the species and quantify the concentration of defects, Doppler broadening spectra of the annihilating γ rays were theoretically calculated using the QMAS (Quantum MAterials Simulator) code,[39–41] which uses valence-electron wavefunctions

determined using the projector augmented-wave (PAW) method.[66,67] To describe the electronic exchange and correlation energies of electrons, the generalized gradient approximation[68] was used. The calculations were carried out on orthorhombic supercells that are equivalent to $4 \times 4 \times 2$ wurtzite cells containing 128 atoms when there is no vacancy. The supercell dimensions were $2\sqrt{3}a_0 \times 4a_0 \times 2c_0$, where $a_0 = 0.3189$ nm and $c_0 = 1.03725$ nm were the lattice parameters. For the supercell that contains a defect, atomic positions in the fixed cell (with the experimental lattice parameters) were optimized computationally. The formalism of the local density approximation[69,70] was used to describe the correlation of $e^- - e^+$.

Localized e^+ at vacancy-type defects may affect the defect configuration and accordingly the corresponding e^+ annihilation.[41] Such effects due to the trapped e^+ can be treated appropriately by the two component density functional theory (TC-DFT) scheme.[69,70] However, different from the case of a Zn vacancy (V_{Zn}) and divacancies comprising a V_{Zn} and an O vacancy in ZnO,[71] the positron annihilation parameters (S, W parameters and positron lifetime) of GaN are only marginally affected.[72] Accordingly, calculations were carried out neglecting the aforementioned effects.

The Doppler broadening spectra for the annihilation of e^+ in DF and various trapped states were calculated, and the directionally averaged (S, W) coordinates for e^+ annihilation at the DF region [(S_{DF}, W_{DF})], V_{Ga} [($S_{V_{Ga}}$, $W_{V_{Ga}}$)], $V_{Ga}V_N$ divacancies [($S_{V_{Ga}V_N}$, $W_{V_{Ga}V_N}$)], $V_{Ga}(V_N)_2$ trivacancies [($S_{V_{Ga}(V_N)_2}$, $W_{V_{Ga}(V_N)_2}$)], $(V_{Ga}V_N)_2$ tetravacancies [($S_{(V_{Ga}V_N)_2}$, $W_{(V_{Ga}V_N)_2}$)], vacancy-impurity complexes like $V_{Ga}O_N$, and so on are shown by open and half-open symbols in Fig. 2 (after Refs. 41, 60, and 73). Here, for directly comparing each calculated (S, W) coordinate and experimentally obtained (S, W), the S parameter was defined as the intensity of the simulated γ-ray spectrum for the energy range of $511\,\text{keV} \pm \Delta E_\gamma$, where $\Delta E_\gamma = 0.76$ keV, around the center of the peak, over the total intensity. The W parameter was calculated for the intensity of the γ ray in the tail of the spectrum ($3.4\,\text{keV} \le |\Delta E\gamma| \le 6.8\,\text{keV}$) over the total intensity.

The assignment and quantification of the vacancy-type defects were carried out as follows. When the samples contain monodefects of vacancy-type (including vacancy-impurity complexes), e^+ annihilate either from the DF state or from the trapped (defect) state. In such a case, (S, W) becomes a weighted average of (S_{DF}, W_{DF}) and (S_{defect}, W_{defect}), where S_{defect} and W_{defect} are characteristic S and W, respectively, of the defect under consideration. Accordingly, experimental (S, W) should lie on a line segment (S_{DF}, W_{DF}) − (S_{defect}, W_{defect}). Here, we emphasize that the slope of the line is also important for identifying the defect species, as experimental data plots commonly suffer from "lower right" shifts.[42–44,57,60,73] Nevertheless, by comparing experimental (S, W) and calculated (S, W) in Fig. 2, the defect species can be identified.

Then, the defect concentration can be estimated from the values of lower and upper dynamic range of PAS measurement,[37] as follows. When the concentration of the defects is less than the lower dynamic range, namely, the detection limit, e^+, implanted in the sample are delocalized in the DF regions, and (S, W) coordinate represents (S_{DF}, W_{DF}). Conversely, when the defect concentration exceeds the upper dynamic range, almost all e^+ are trapped by

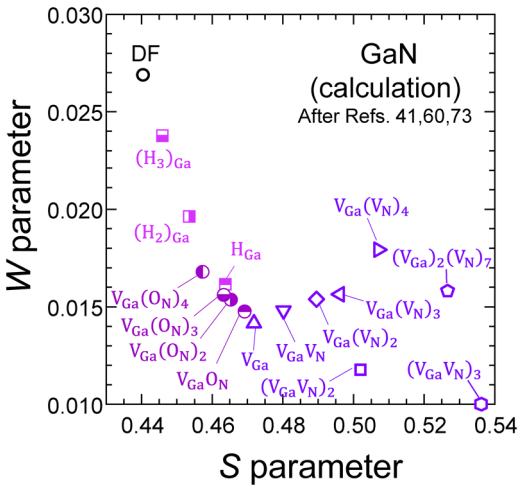

FIG. 2. Calculated (S, W) values[41,60,73] using the QMAS code for positron annihilation in GaN at the defect-free (DF) region (delocalized state) (circle), V_{Ga} (upward triangle), $V_{Ga}V_N$ (downward triangle), $V_{Ga}(V_N)_2$ (diamond), and so on. [Calculated data plots are reproduced with permission from Ishibashi and Uedono, J. Phys. Conf. Ser. **505**, 012010 (2014). Copyright 2014 IOP Publishing LLC;[41] Uedono *et al.*, J. Cryst. Growth **448**, 117 (2016). Copyright 2016 Elsevier B.V.;[60] and Uedono *et al.*, Phys. Status Solidi B **255**, 1700521 (2018). Copyright 2017 WILEY-VCH Verlag GmbH & Co.[73]].

the defects and (S, W) represents (S_{defect}, W_{defect}).[37] The concentration of the defects can eventually be estimated by placing a logarithmic gauge between (S_{DF}, W_{DF}) and (S_{defect}, W_{defect}), which correspond to the lower and upper limits of the dynamic range, respectively. The dynamic range of PAS measurement for V_{Ga} is approximately between 10^{15} and $10^{18}\,\text{cm}^{-3}$ in n-GaN and approximately between 10^{16} and $10^{19}\,\text{cm}^{-3}$ in semi-insulating and p-GaN, as the trapping coefficient of e^+ at negative vacancies (typically $\approx 10^{15} - 10^{16}\,\text{s}^{-1}$) is an order of magnitude higher than that at neutral vacancies (typically $\approx 10^{14} - 10^{15}\,\text{s}^{-1}$) at 300 K (Ref. 37). Accordingly, the concentration of V_{Ga} ([V_{Ga}]) can be estimated from the values of (S_{DF}, W_{DF}) and ($S_{V_{Ga}}$, $W_{V_{Ga}}$) coordinates. In this article, 10^{15} and $10^{18}\,\text{cm}^{-3}$, respectively, in n-GaN and 10^{16} and $10^{19}\,\text{cm}^{-3}$, respectively, in semi-insulating and p-GaN (Ref. 37) were used.

For counterchecking the defect concentration, characteristic S and positron diffusion length (L_+) in each layer of epitaxial structures were determined by using a monoenergetic e^+-beam,[34–38] by which the mean implantation depth of e^+ can be controlled. The analysis[74] is based on solving the diffusion equation of e^+ as a function of acceleration energy E using the initial implantation profile. Here, L_+ can be used as a measure of gross concentration of e^+ trapping and scattering centers because both of them shorten L_+. In a three-dimensional (3D) space, L_+ is likely close to an inverse third root of the defect concentration. The scattering centers are positively charged and neutral point defects such as V_N, interstitials (Ga_i and N_i), and certain complexes. The relationship between S and E was analyzed by a computer program named VEPFIT developed by van Veen *et al.*[74] The one-dimensional (1D) diffusion

model of e^+ is expressed by[33]

$$D_+ \frac{d^2}{dz^2} n(z) - \kappa_{\text{eff}}(z) n(z) + P(z, E) = 0, \quad (6)$$

where D_+ is the diffusion coefficient of e^+, $n(z)$ is the probability density of e^+ at a distance z from the surface, $\kappa_{\text{eff}}(z)$ is the effective escape rate of e^+ from the diffusion process, and $P(z, E)$ is the implantation profile of e^+. Then, $L_+(z)$ is given by

$$L_+(z) = \sqrt{D_+/\kappa_{\text{eff}}(z)}. \quad (7)$$

In the fitting procedure, a homogeneous distribution of defects was assumed. The S–E curve was fitted to the following equation:

$$S(E) = S_e F_e(E) + S_S F_S(E) + \sum S_i F_i(E), \quad (8)$$

where $Fe(E)$, $Fs(E)$, and $Fi(E)$ are the fractions of epithermal (non-thermalized) positrons annihilated at the surface, that of positrons annihilated at the surface, and that of positrons annihilated in the ith block, respectively $[F_e(E) + F_s(E) + \Sigma F_i(E) = 1]$. The values of S_e, S_s, and S_i are characteristic S parameters for the respective annihilation events. The analytical procedures used in this study are similar to those described in Ref. 36.

The monoenergetic e^+-beam line used to measure the Doppler broadening spectra of the annihilating γ ray as a function of E with a Ge detector was the same as in Refs. 36, 38, 42–44, 57, 60, 62, 63, and 73. A spectrum with 3×10^6 counts was measured at each E. The low-momentum portion for determining the S parameter was defined for the energy range of $511\,\text{keV} \pm \Delta E_\gamma$, where $\Delta E_\gamma = 0.76\,\text{keV}$, around the center of the peak, over the total counts. The W parameter was calculated for the annihilation events in the tail of the spectra ($3.4\,\text{keV} \le |\Delta E\gamma| \le 6.8\,\text{keV}$) over the total counts. For semi-insulating and p-type GaN, the samples were illuminated with the 325.0 nm line of a He–Cd laser during the measurement, in order to supply electrons to neutral or positively charged levels[73] for increasing the positron trapping probability.

To examine the annihilation characteristics of positrons in detail, the coincidence detection system[36] was also used. The spectra with about 5×10^6 counts were obtained and then characterized using the S and W parameters.

C. Steady-state and time-resolved photoluminescence measurements

Steady-state and time-resolved PL measurements were carried out under the weak-excitation conditions[22,24–28] defined in Sec. I, in order to underline the MGR processes.[5] Steady-state PL was excited using the 325.0 nm line of a cw He–Cd laser with the power density of $38\,\text{W cm}^{-2}$. TRPL measurement was carried out using approximately 110 fs pulses of a frequency-tripled mode-locked Al_2O_3:Ti laser ($\lambda = 267\,\text{nm}$) with the energy density of $120\,\text{nJ cm}^{-2}$ per pulse, of which repetition rate was decreased by a pulse picker to 8 MHz. The spot diameter and estimated n_{excited} were 100 μm and a few times $10^{16}\,\text{cm}^{-3}$, respectively, when τ_{PL} was 1 ns. We note that this n_{excited} was the highest because $\tau_{\text{PL}}^{\text{RT}}$ distributed from 1 ns (***A***) down to 2 ps (***R***), which will be shown later. Under these excitation conditions, n_{excited} was far less than the majority carrier concentration and also far below the threshold for maintaining negligible classical[17,18] and trap-assisted[19] Auger–Meitner nonradiative recombination processes at 300 K. It is also important to note that the measured $\tau_{\text{PL}}^{\text{RT}}$ increased with increasing excitation power density, for example, from 220 to 510 ps by increasing the energy density from 0.2 to $120\,\text{nJ cm}^{-2}$ for one of the samples (***A***), indicating that the weak-excitation conditions[22,24–28] were maintained and the increase in $\tau_{\text{PL}}^{\text{RT}}$ reflected a progressive saturation of MGRCs. One of the other examples can be found in a literature,[75] in which $\tau_{\text{PL}}^{\text{RT}}$ increased from 42 to 170 ps with increasing the laser energy density from 4 to $600\,\text{nJ cm}^{-2}$.

The TRPL signals were collected using a streak camera. The acquisition was carried out using either a synchro-scan mode with the highest temporal resolution of 1 ps or a conventional slow-scan mode. The temporal decay signals for the NBE emission of GaN showed a single- or precisely multiple-exponential line shape. The appearance of multiple decay components most likely arose from spatial inhomogeneity in $\tau_{\text{PL}}^{\text{RT}}$, i.e., N_{MGRC} and/or the presence of any quantum confined transition such as discrete transitions taking place in strain or structural singularities[76–80] within the excitation volume. Because spectrally (energy) resolved decay signals across the photon energy range for the NBE emission did not show energy dependences in all samples at 300 K, spatial inhomogeneity in N_{MGRC} within the excitation volume[79] appears to be the most probable cause. Nevertheless, most of the PL decay signals were well fitted using a single- or bi-exponential line shape function,

$$I(t) = A_1 \exp(-t/\tau_1) + A_2 \exp(-t/\tau_2), \quad (9)$$

where $I(t)$ is the PL intensity at time t. $A_1(A_2)$ and $\tau_1(\tau_2)$ are the pre-exponential constant and lifetime, respectively, for the fast (slow) decay component. The value of τ_1 is used as a principal $\tau_{\text{PL}}^{\text{RT}}$ representative because cw $\eta_{\text{int}}^{\text{NBE}}$ and thereby PL intensity are usually limited by τ_1. Contribution of slow decay components such as τ_2 will be discussed later. Because $\tau_{\text{PL}}^{\text{RT}}$ in bulk 3D GaN is approximately 40 ns,[22,23] τ_{MGR} at room temperature can be derived from Eq. (5) using the measured $\tau_{\text{PL}}^{\text{RT}}$. Practically, $\tau_{\text{PL}}^{\text{RT}}$ nearly agrees with room-temperature τ_{MGR} in bulk semiconductors without quantum confinement structures or localization mechanisms.

III. RESULTS AND DISCUSSION

A. n-type GaN

1. Species and capture coefficients of vacancy-type defects

Measured (S, W) for n-GaN supplied by ***A***, ***H***, and ***N*** are shown by black, dark gray, and carmine closed symbols, respectively, in Fig. 3. Error bars are not given on all S–W plots hereafter because the experimental errors to determine S and W were both less than 0.1%. Each supplier ID is shown by an italic outline character on a colored square background in the figures. Some of the calculated[41,60,73] (S, W) shown in Fig. 2 are plotted by open symbols for identifying the vacancy-type defect species. For comparison, previously measured[24,25] (S, W) values for the GaN

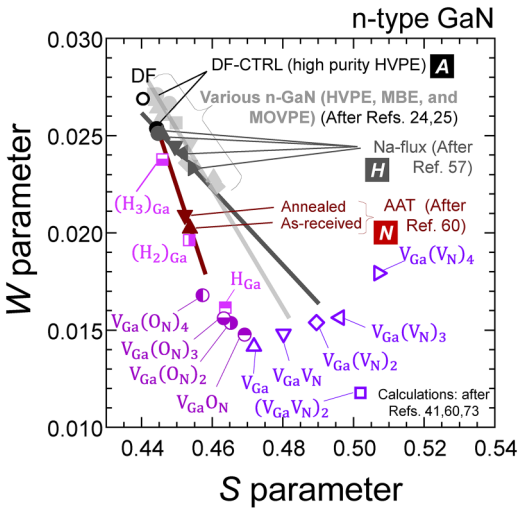

FIG. 3. Measured (S, W) for n-GaN supplied by ***A***, ***H,*** and ***N*** (closed black, dark gray,[57] and carmine[60] symbols, respectively). Error bars are not given on all S–E plots hereafter because the experimental errors for the determination of both S and W were less than 0.1%. Each supplier ID is shown by an italic outline character on a colored square background in the figure. The calculated[41,60,73] (S, W) coordinates already shown in Fig. 2 are plotted by open symbols for determining the vacancy defect species. For comparison, previously measured[24,25] (S, W) for the GaN samples of various origins, which have been grown by HVPE, MOVPE, and molecular beam epitaxy (MBE), are displayed by closed light gray symbols. [Calculated data plots are reproduced with permission from Ishibashi and Uedono, J. Phys. Conf. Ser. **505**, 012010 (2014). Copyright 2014 IOP Publishing LLC;[41] Uedono *et al.*, J. Cryst. Growth **448**, 117 (2016). Copyright 2016 Elsevier B.V.;[60] and Uedono *et al.*, Phys. Status Solidi B **255**, 1700521 (2018). Copyright 2017 WILEY-VCH Verlag GmbH & Co.[73] Experimental data plots are reproduced with permission from Chichibu *et al.*, J. Appl. Phys. **123**, 161413 (2018). Copyright 2018 AIP Publishing LLC;[25] Uedono *et al.*, J. Cryst. Growth **475**, 261 (2017). Copyright 2017 Elsevier B.V.;[57] and Uedono *et al.*, J. Cryst. Growth **448**, 117 (2016). Copyright 2016 Elsevier B.V[60]].

samples of various origins, which have been grown by HVPE, MOVPE, and molecular-beam epitaxy (MBE), are displayed by closed light gray symbols. The (S, W) values of HVPE GaN (supplier ***A***, defined "defect-free-control: DF-CTRL"), of which quality is equivalent to the highest quality sample "C0" in Ref. 22, measured in the present study (closed black circle) and in 2012 (closed light gray circle) are mismatched, especially in W parameter, and both plots exhibited larger S than calculated S_{DF} (open black circle).

The difference in W likely originates from improved sensitivity of the Ge detector used in the present study, which improved the detection limit and, thus, gave rise to the decrease in the baseline, resulting in the decrease in the signal of the spectral tails (wing portions). The distinct "lower right" shifts of the measured (S, W) of DF-CTRL with respect to calculated (S_{DF}, W_{DF}) in the present study could be due to several reasons such as the limitations of first-principle calculations applied to Doppler broadening spectra, temperature-dependent differences between the modeling and experimental conditions, the experimental background, and/or the energy resolutions of our Ge detectors. Nevertheless, the measured (S, W) coordinates of DF-CTRL most likely represent "experimental" (S_{DF}, W_{DF}) in the present study (black) and in 2012 (light gray) based on the following reasons: (i) DF-CTRL showed the smallest S and largest W; (ii) DF-CTRL exhibited long τ_{PL}^{RT} (for the NBE emission) of 1.1 ns;[22] and (iii) L_+ of DF-CTRL was 116 nm (Ref. 22) that supported gross concentration of e^+ trapping and scattering centers (N_{defect}^{gross}) less than 10^{15} cm^{-3} since 3D average distance between adjacent defects for $N_{defect}^{gross} = 10^{15}$ cm^{-3} is 100 nm. The value of $N_{defect}^{gross} \leq 10^{15}$ cm^{-3} almost agrees with the detection limit of PAS for n-GaN,[37] as described in Sec. II B.

Because experimental data plots commonly suffer from lower right shifts, the slope of the approximated line for the (S, W) coordinates is important to determine the defect species. As the slope of an approximated line for the light gray (S, W) plots nearly agreed[25] with the slope of a line connecting the calculated (S_{DF}, W_{DF}) and ($S_{V_{Ga}V_N}$, $W_{V_{Ga}V_N}$), major vacancy-type defects in a variety of n-GaN grown from the vapor phase by HVPE, MOVPE, and MBE were identified to be $V_{Ga}V_N$ (Ref. 25). Consistently, (S, W) coordinates for the GaN samples from suppliers ***B***, ***C***, ***E***, ***F***, and ***G*** were close to (S, W) of DF-CTRL (supplier ***A***) and aligned on a virtual line with the slope of a line connecting the calculated (S_{DF}, W_{DF}) and ($S_{V_{Ga}V_N}$, $W_{V_{Ga}V_N}$). Because of the large number of samples supplied, the data plots for ***B***, ***C***, ***E***, ***F***, and ***G*** are not shown for avoiding congestion.

Different from GaN films and layers grown from vapor phase, major vacancy-type defects in Na-flux GaN (***H***) have been revealed to be larger vacancy clusters like $V_{Ga}(V_N)_3$ because the approximated line for the experimental (S, W) coordinates of ***H*** (thick dark gray line) has been parallel to a virtual line connecting the calculated (S_{DF}, W_{DF}) and ($S_{V_{Ga}(V_N)_3}$, $W_{V_{Ga}(V_N)_3}$).[57] It is interesting to note that the size of the major intrinsic point defects in the bulk GaN crystals grown from the melt at high P_g of the order of 4–10 MPa (Ref. 57) is much larger than that for the epitaxial films ($V_{Ga}V_N$) grown from the vapor phase at P_g lower than 0.1 or 0.01 MPa.

Major vacancy-type defects in AAT GaN (***N***) has been identified to be H_{Ga} and/or $V_{Ga}(O_N)_{3-4}$ because the approximated line for (S, W) coordinates of ***N*** and experimental (S_{DF}, W_{DF}) of DF-CTRL was parallel to the virtual line connecting the calculated (S_{DF}, W_{DF}) and ($S_{H_{Ga}}$, $W_{H_{Ga}}$) or ($S_{V_{Ga}(O_N)_{3\sim4}}$, $W_{V_{Ga}(O_N)_{3\sim4}}$).[60] The assignment is consistent with the previous report[81] on the defect characterization of BAT GaN. The reason why V_{Ga} buried by multiple H atoms such as $(H_{2-3})_{Ga}$ was excluded was that e^+ was not fully trapped in the case of AAT crystals (***N***) that exhibited L_+ of 60–90 nm: if the major defects were $(H_2)_{Ga}$, L_+ should be much shorter[22,24,25] because $(H_2)_{Ga}$ concentration would be close to the upper dynamic range being 10^{19} cm^{-3}, as shown in Fig. 3, and e^+ would be fully trapped.

In Fig. 4, relationships between τ_{PL}^{RT} and N_{MGRC} ($\tau_{PL}^{RT} - N_{MGRC}$ relationships) of common MGRCs in n-GaN, namely, Fe on Ga site ($Fe_{Ga}^{3+/2+}$) (Ref. 30), $C_N^{0/-}$ (Ref. 29), and $V_{Ga}V_N$ (Ref. 25), are drawn by green, red, and black curves, respectively, using Eqs. (3) and (5), where $\tau_R = 40$ ns (Refs. 22 and 23) and C_p values of 5×10^{-8} (Ref. 30), 2×10^{-7} (Ref. 29), and 6×10^{-7} (Ref. 25) cm^3 s^{-1}, respectively, are used. We note that Reshchikov[32] has reported similar large C_p of 3.7×10^{-7} cm^3 s^{-1} for the

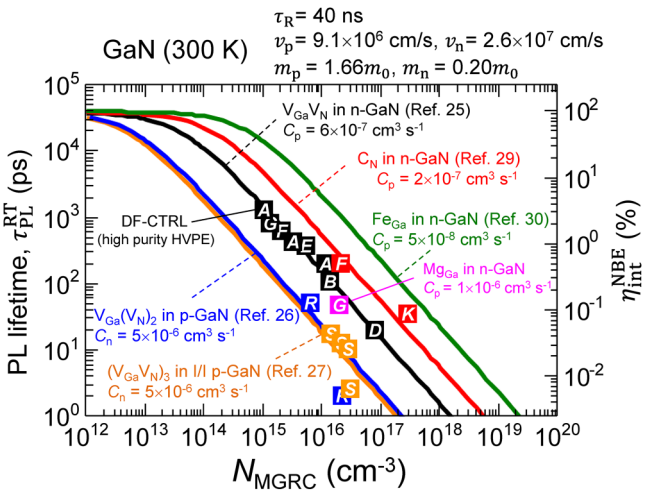

FIG. 4. $\tau_{PL}^{RT} - N_{MGRC}$ relationships for common MGRCs in n-GaN: $Fe_{Ga}^{3+/2+}$ (Ref. 30), C_N (Ref. 29), and $V_{Ga}V_N$ (Ref. 25). They are drawn by green, red, and black curves, respectively, using Eqs. (3) and (5), where $\tau_R = 40$ ns (Refs. 22 and 23) and C_p values of 5×10^{-8} (Ref. 30), 2×10^{-7} (Ref. 29), and 6×10^{-7} (Ref. 25) $cm^3\,s^{-1}$, respectively, are used. By using $v_{th} = v_p = 9.1 \times 10^6\,cm \cdot s^{-1}$ that is obtained from hole effective mass (m_p) of $1.66m_0$, σ_p are 6×10^{-15}, 2×10^{-14}, and $7 \times 10^{-14}\,cm^2$, respectively. Here, $Fe_{Ga}^{3+/2+}$ and $C_N^{0/-}$ are known as E3 (Ref. 82) and H1 (Ref. 54) traps, respectively. Blue and orange curves are $\tau_{PL}^{RT} - N_{MGRC}$ relationships for common MGRCs in p-type GaN: $V_{Ga}(V_N)_2$ (Ref. 26) and $(V_{Ga}V_N)_3$ (Ref. 27), respectively. For both vacancy clusters, nearly equal C_n value of $5 \times 10^{-6}\,cm^3\,s^{-1}$ (Refs. 26 and 27) is used. By using $v_{th} = v_n = 2.6 \times 10^7\,cm \cdot s^{-1}$ that is obtained from electron effective mass (m_n) of $0.20m_0$, σ_n is $2 \times 10^{-13}\,cm^2$. In the figure, corresponding $\eta_{int}^{NBE}(= \tau_{PL}^{RT}/\tau_R)$ at 300 K is shown on right y-axis. Measured τ_{PL}^{RT} of n- and p-type GaN (suppliers ***A***, ***B***, ***D***, ***E***, ***F***, ***G***, ***K***, ***R***, and ***S***) are plotted by italic outline characters on colored-square background. [Presentation style partially reproduced with permission from Chichibu *et al.*, J. Appl. Phys. **123**, 161413 (2018). Copyright 2018 AIP Publishing LLC].[25]

$C_N^{0/-}$ center. By using $v_{th} = v_p = 9.1 \times 10^6\,cm\,s^{-1}$ that is obtained from hole effective mass (m_p) of $1.66m_0$, corresponding σ_p are 6×10^{-15}, 2×10^{-14}, and $7 \times 10^{-14}\,cm^2$, respectively. Here, $Fe_{Ga}^{3+/2+}$ and $C_N^{0/-}$ are known as E3 (Ref. 82) and H1 (Ref. 54) traps, respectively. In the figure, corresponding $\eta_{int}^{NBE}(= \tau_{PL}^{RT}/\tau_R)$ at 300 K is shown on the right y-axis. Herein, we propose the use of $\tau_{PL}^{RT} - N_{MGRC}$ curves in Fig. 4 as calibrating measures for quantifying (or semi-quantifying) the concentrations of respective MGRCs below the detection limits of PAS (or SIMS for [C]). For substitutional impurities in Si, a standardization of B, P, and low-level C concentrations well below the detection limits of SIMS measurements has been realized by using a low-temperature PL measurement.[83,84] In the present case, the concentrations of native defects could be quantified, although the definition of the weak-excitation conditions[22,24–28] may become more important.

Blue and orange curves in Fig. 4 are $\tau_{PL}^{RT} - N_{MGRC}$ relationships for p-GaN, and the details will be given in Sec. III B. In Fig. 4, measured τ_{PL}^{RT} (fast component τ_1) of n-GaN samples (suppliers ***A***, ***B***, ***D***, ***E***, ***F***, ***G***, and ***K***) and p-GaN samples (suppliers ***R*** and ***S***) are plotted by italic outline characters on colored-square background. In the following, several experimental data are explained more precisely.

2. MOVPE and HVPE GaN

For the GaN samples grown from the vapor phase (HVPE and MOVPE) except for ***D***, τ_{PL}^{RT} was principally limited by $[C_N^{0/-}]$ when [C] was higher than about $10^{16}\,cm^{-3}$ and by $[V_{Ga}V_N]$ for low [C] samples, as follows. Steady-state PL spectra of MOVPE GaN (***F***) of different [C], namely, 2×10^{15} and $2 \times 10^{16}\,cm^{-3}$, are shown in Figs. 5(a) and 5(b), respectively. In each panel, upper (black) and lower (red) curves show the spectra at 12 and 300 K, respectively. The PL intensity (y-) axis has a unit of count per second (cps), and the spectra can be directly compared with those at different temperatures or other samples throughout this article, except for those shown using arbitrary units. As shown, both epilayers exhibited distinct NBE PL peaks and shoulders originating from the recombination of free A-excitons (FX_A) at 3.478 eV, recombination of excitons bound to a neutral donor (DBEs) at 3.472 eV, and their LO phonon replicas at the energies higher than 3.2 eV at 12 K. In addition, weak luminescence bands called "blue luminescence (BL)" due to the transition of an electron from the conduction band to a $C_N^{+/0}$ center[32] or from a deep-donor state of carbon on a Ga site (C_{Ga})[79] at around 2.9 eV (carbon-blue), "YL" at around 2.2 eV (Refs. 45–47, 51, and 86), and "red luminescence (RL)" at around 1.8 eV (Ref. 87) were detected. By using the first-principles calculations, Reshchikov *et al.*[87] have suggested that V_N are the origin of the RL band. In this context, the appearance of RL implies noticeable $[V_N]$ in these epilayers. There could be two independent origins for the YL band: one is the transition of an electron in the conduction band (or bound to a shallow donor) to an acceptor-like $C_N^{0/-}$ deep center[47,54] and the other is the emission due to the complex of a V_{Ga} and a donor impurity such as an O on a N site (O_N), $V_{Ga}O_N$.[47,51] It is noted that room-temperature YL intensity increased and NBE emission intensity decreased with the increase in [C] from 2×10^{15} to $2 \times 10^{16}\,cm^{-3}$. The results indicate that most of C substitute N sites to form C_N and act as DRCs, being consistent with the $C_N^{0/-}$ transition model for the YL band.[47]

Consistent with the steady-state PL results, τ_{PL}^{RT} of the NBE emission decreased from 0.6 to 0.2 ns with increasing [C], as indicated beside the integrated spectral TRPL decay signals for the NBE emissions of the MOVPE layer (supplier ***F***) with [C] of 2×10^{15} and $2 \times 10^{16}\,cm^{-3}$ in Figs. 5(c) and 5(d), respectively. The τ_{PL}^{RT} value (0.2 ns) of ***F*** with $[C] = 2 \times 10^{16}\,cm^{-3}$ is plotted by red ***F*** near the center in Fig. 4. The τ_{PL}^{RT} value almost agreed with the value on the calculated red curve for $[C_N] = 2 \times 10^{16}\,cm^{-3}$, while τ_{PL}^{RT} of ***F*** with $[C] = 2 \times 10^{15}\,cm^{-3}$ (0.6 ns) was shorter than the calculated value for $[C_N] = 2 \times 10^{15}\,cm^{-3}$ being approximately 2.5 ns (crossing between the red line and $N_{MGRC} = 2 \times 10^{15}\,cm^{-3}$). In such low [C] samples, τ_{PL}^{RT} was no longer limited by $[C_N]$ and, therefore, most likely limited by $[V_{Ga}V_N]$ because the major vacancy defects in n-GaN grown from the vapor phase is $[V_{Ga}V_N]$,[25] as revealed from Fig. 3. Then, $[V_{Ga}V_N]$ can be estimated from the crossing between the black curve and $\tau_{PL}^{RT} = 0.6$ ns to be approximately $2 \times 10^{15}\,cm^{-3}$ (black ***F*** located on the black curve in Fig. 4). Because $[V_{Ga}V_N] = 2 \times 10^{15}\,cm^{-3}$ nearly agrees with the detection limit (lower dynamic range) of PAS in n-GaN,[37] the (S, W) coordinate

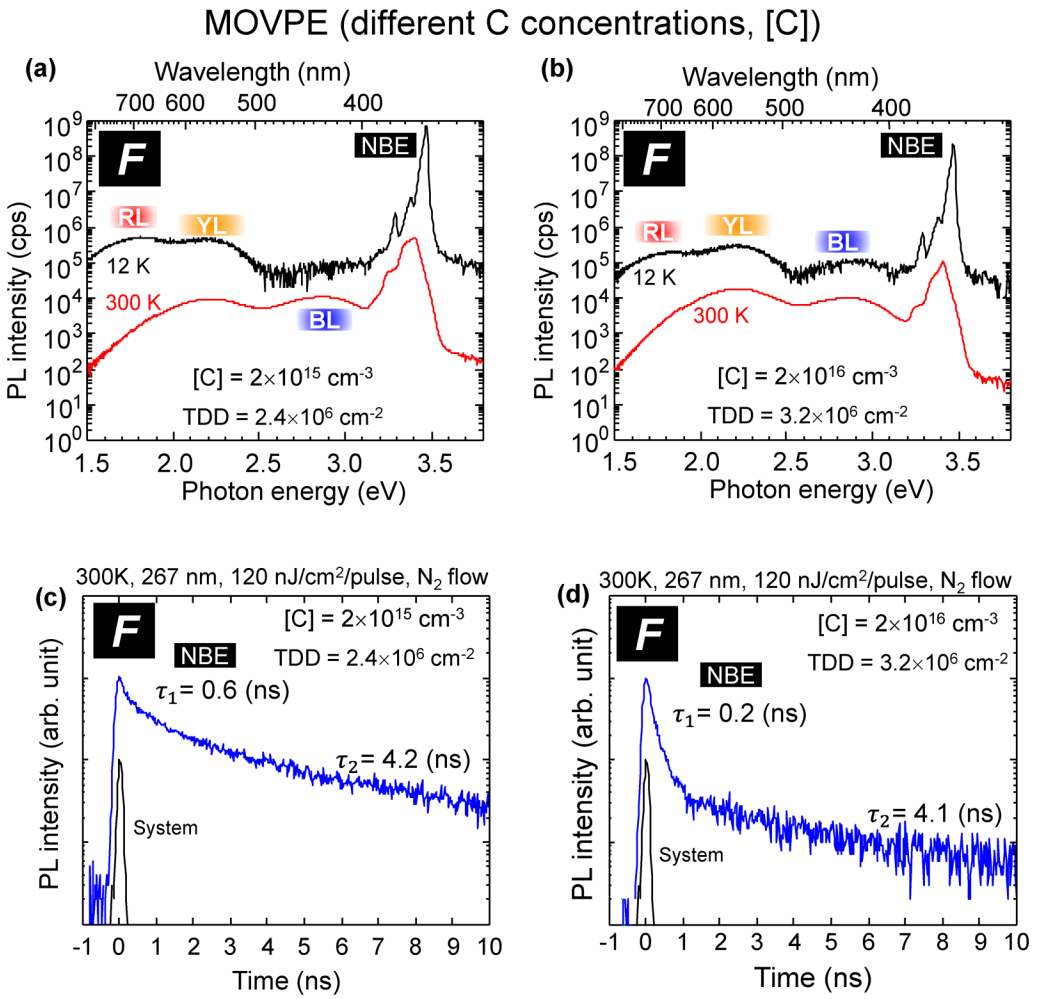

FIG. 5. Steady-state PL spectra of MOVPE GaN (***F***) with [C] of (a) 2×10^{15} and (b) 2×10^{16} cm^{-3}. In each panel, upper (black) and lower (red) curves show the spectra at 12 and 300 K, respectively. The PL intensity (*y*-) axis has a unit of count per second (cps), and the spectra can be compared with those at different temperatures or other samples. The NBE emission includes free and bound excitons and their phonon replicas. BL, YL, and RL indicate the blue luminescence,[32,85] yellow luminescence,[45–47,51,86] and red luminescence[87] bands, respectively. Integrated spectral TRPL decay signals for the NBE emissions measured at 300 K of the MOVPE GaN (***F***) with [C] of (c) 2×10^{15} and (d) 2×10^{16} cm^{-3}. The signal denoted by "System" shows the overall system response. The decay curves were fitted using a bi-exponential line shape function [Eq. (9)]. For plotting the data on Fig. 4, τ_1 values are used as principal τ_{PL}^{RT} representative.

almost overlaps with the experimental (S_{DF}, W_{DF}). For avoiding congestion of data plots, the (S, W) data are not plotted in Fig. 3.

As described in the preceding paragraph, either [C] or [$V_{Ga}V_N$] limited τ_{PL}^{RT} of MOVPE epilayers depending on the reciprocal numbers of $C_p \cdot N_{MGRC}$. The dominance of [$V_{Ga}V_N$] in limiting τ_{PL}^{RT} was observed in thick HVPE layers or sliced substrates, which principally contain low [C]. In Figs. 6(a) and 6(b), integrated spectral TRPL decay signals at 300 K for the NBE emission of the HVPE GaN from suppliers ***A*** and ***B***, respectively, are shown. In both samples, [C] was less than the detection limit of the particular SIMS measurement ($\sim 3 \times 10^{15}$ cm^{-3}), which predicts τ_{PL}^{RT} longer than 2 ns (see the red curve in Fig. 4). However, the samples exhibited relatively short and different τ_{PL}^{RT} of 0.43 and 0.11 ns, respectively, although [C] and TDD are nearly the same. The result indicates the dominance of [$V_{Ga}V_N$] in limiting τ_{PL}^{RT}. Accordingly, symbols ***A*** (0.43 ns) and ***B*** (0.11 ns) are plotted on the black curve in Fig. 4 at the crossings with respective τ_{PL}^{RT} values. Then, each [$V_{Ga}V_N$] is obtained from the intersection between a perpendicular line from the symbol and horizontal axis. The obtained [$V_{Ga}V_N$] values are lower than approximately 1.3×10^{16} cm^{-3} for both samples, and therefore, (S, W) coordinates almost overlap with the experimental (S_{DF}, W_{DF}) again.

In addition to $C_N^{0/-}$ and $V_{Ga}V_N$, C_p of $Mg_{Ga}^{0/-}$ was obtained from MOVPE GaN, as supplier ***G*** accidentally gave us an n-GaN epilayer containing Mg impurity of approximately 2×10^{16} cm^{-3}, in addition to a high-purity epilayer with $\tau_{PL}^{RT} = 0.8$ ns (black symbol

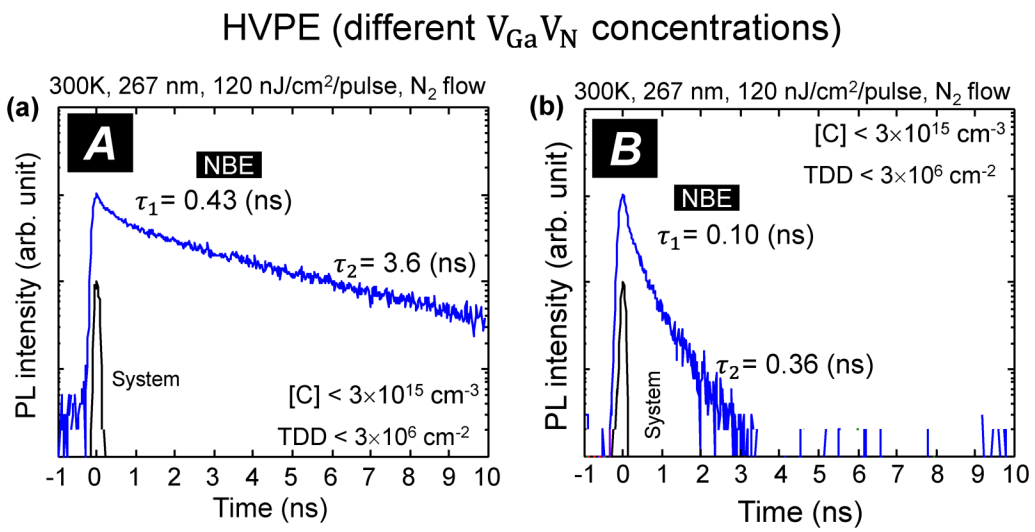

FIG. 6. Integrated spectral TRPL decay signals at 300 K for the NBE emissions of the HVPE GaN from suppliers (a) ***A*** and (b) ***B***. The signal denoted by "System" shows the overall system response. In both samples, [C] was less than the detection limit of the particular SIMS measurement (~3×10^{15} cm^{-3}), which predicts τ_{PL}^{RT} longer than 2 ns when $\left[C_N^{0/-}\right]$ limits the lifetime (see Fig. 4). The decay curves were fitted using a bi-exponential line shape function [Eq. (9)], and τ_1 values are used as representative τ_{PL}^{RT}. In these low [C] GaN, τ_{PL}^{RT} is most likely limited by [$V_{Ga}V_N$].

G in Fig. 4). Because the Mg-containing sample showed n-type conductivity, τ_{PL}^{RT} value of 50 ps (plotted by magenta symbol in Fig. 4) gave C_p value of approximately 1×10^{-6} cm^3 s^{-1} ($\sigma_p = 1.1 \times 10^{-13}$ cm^2). This large C_p exactly agrees with the data reported by Reshchikov.[32]

3. GaN crystals grown from the liquid and supercritical states

Different from the GaN samples grown from the vapor phase, the results shown in Fig. 3 indicated that GaN crystals grown by the Na-flux method contained larger-size vacancy clusters such as $V_{Ga}(V_N)_3$ (Ref. 57) and those grown using the supercritical NH_3 (BAT and AAT) contained vacancy-impurity complexes such as H_{Ga} or $V_{Ga}(O_N)_{3-4}$ (Ref. 60). Such vacancy complexes also influence τ_{PL}^{RT}. PL spectra of the Na-flux[56] GaN crystals (supplier ***J***, grown using Na–Ga melt[58] and Na vapor[58,59]) and LPE GaN wafer (supplier ***K***) are shown in Figs. 7(a) and 7(b), respectively. As shown by top two traces in Fig. 7(a),[59] the PL spectrum at 9 K (293 K) of the crystal grown using the Na–Ga melt[58] exhibited a broad NBE emission band with the peak at 3.470 eV (3.425 eV), of which full-width at half-maximum (FWHM) was about 67 meV (150 meV). According to the fact that the FWHM value of the NBE emission often reflects the bandgap broadening caused by the residual impurities,[88,89] the residual electron concentration is estimated to be in the range of high 10^{19} cm^{-3}. The PL spectra also exhibited broad emission bands at around 3.3 and 2.9 eV. Because similar emission bands have been reported in C, Mg, or Zn-doped GaN,[86,90,91] the origins of the 3.3 and 2.9 eV bands are tentatively assigned as a conduction band to acceptor (FA) transition and a donor-to-acceptor pair (DAP) transition, respectively. The origins will be discussed later because both bands appear to suffer from spectral broadenings caused by high concentration impurities.

Conversely to the GaN crystal grown using the Na–Ga melt, the emission bands due to DLs were absent and the FWHM value for the NBE peak was as small as 1.3 meV at 9 K for the crystal grown using Na vapor,[58] as shown by bottom black trace in Fig. 7(a).[59] More precisely, PL peaks originating from radiative recombinations of free A- and B-excitons (FX_A and FX_B, respectively) and those bound to a neutral donor (DBE peaks $I_{2,A}$ and $I_{2,B}$, respectively) were observed. From the peak energy (3.414 eV) and FWHM (45 meV) of the NBE emission at 293 K, the electron concentration is estimated to be mid-10^{17} cm^{-3}. Since O concentration quantified by the SIMS measurement was in the order of 10^{17} cm^{-3}, O appears to be the major donor impurity. The concentrations of other impurities such as Si and C were lower than the detection limits. All data indicate superior properties of GaN crystals grown using Na vapor[58,59] compared with those using the Na–Ga melt.[57]

The PL spectrum at 12 K of the Ge-doped (3×10^{18} cm^{-3}) LPE GaN (***K***) exhibited the NBE (a DBE) peak at 3.472 eV and its LO phonon replicas at the energies higher than 3.2 eV, as shown in Fig. 7(b). The FWHM value for the DBE peak (~14 meV) was intermediate among the Na-flux GaN crystals (***J***) grown using the Na–Ga melt and Na vapor,[58,59] reflecting the intermediate donor impurity concentration. In addition to the NBE peak, distinct ultraviolet luminescence (UVL) band at around 3.26 eV was observed, which most probably originate from a free electron or a shallow donor to a Mg_{Ga} acceptor transition.[86,91] Moreover, low-energy tail of the UVL band (BL band) and distinct "green luminescence (GL)" band were observed. Because [C] of the GaN crystal (***K***) quantified using SIMS measurement was 3×10^{17} cm^{-3}, which was the highest among the samples measured in this study, the BL

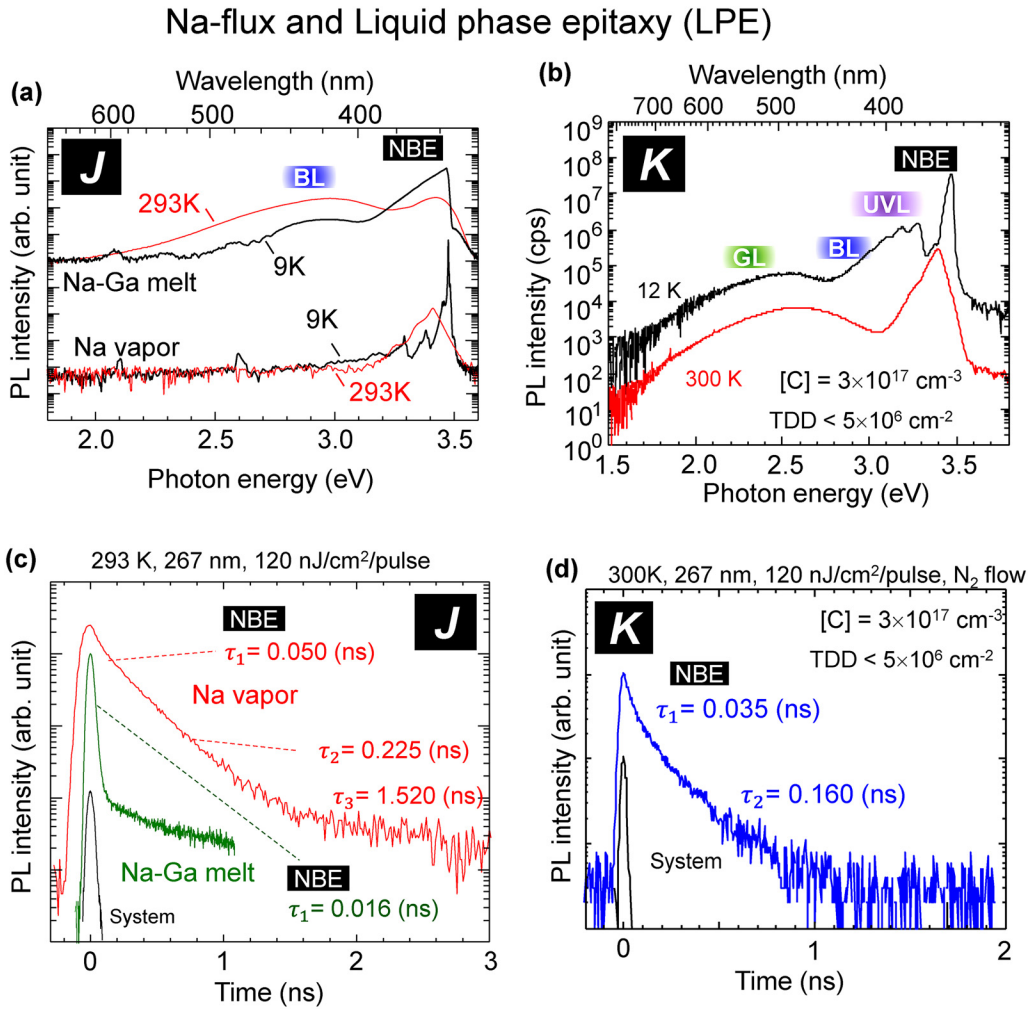

FIG. 7. PL spectra of (a) Na-flux GaN crystals from supplier ***J*** grown using Na–Ga melt and Na vapor[58,59] and (b) LPE GaN wafer from supplier ***K***. Room-temperature integrated spectral TRPL decay signals measured for the NBE emissions of (c) the Na-flux GaN (**J**) grown using Na–Ga melt and Na vapor[59] and (d) LPE GaN (***K***) containing high concentration carbon ([C] = 3 × 10^{17} cm^{-3}). The signal denoted by "System" shows the overall system response. The decay curves were fitted using a bi-exponential (or tri-exponential) line shape function [Eq. (9)], and τ_1 values are used as representative τ_{PL}^{RT}. [The data in (a) and (c) are reproduced with permission from Onuma *et al.*, Appl. Phys. Express **2**, 091004 (2009). Copyright 2009 IOP Publishing LLC].[59]

likely originates from $C_N^{+/0}$ (Ref. 32) or C_{Ga} (Ref. 85) and GL may include a high-energy shifted YL band that mainly originates from $C_N^{0/-}$ (Refs. 47 and 54). Another well-known origin for the GL band is V_N (Ref. 87), which does not contradict the present finding that-GaN crystals grown from liquid phase contained V_N-rich vacancy clusters like $V_{Ga}(V_N)_3$ (Ref. 57) instead of $V_{Ga}V_N$.

Integrated spectral TRPL decay signals at room temperature for the NBE emissions of Na-flux GaN (***J***) grown using the Na–Ga melt and Na vapor[59] are shown in Fig. 7(c). Consistent with the well-resolved NBE emissions displayed in Fig. 7(a), τ_{PL}^{RT} of the GaN crystal grown using Na vapor (50 ps) was more than three times the crystal grown using the Na–Ga melt (16 ps).[59] Because [C] was lower than the detection limit of the SIMS measurement and YL band originating from $C_N^{0/-}$ (Refs. 47 and 54) was not observed in the lower trace of Fig. 7(a), τ_{PL}^{RT} is most likely limited by the concentration of intrinsic point defects. Unfortunately, typical dimensions of the GaN crystals (***J***) were 1- to 5-mm-long along the *c*-axis and 300-μm-diameter surrounded by naturally formed six *m*-planes,[58,59] which were too small for PAS measurements. Therefore, the τ_{PL}^{RT} values of ***J*** are not displayed in Fig. 4. It is noted from Fig. 7(c) that the appearance of three decay components indicates the presence of at least three major domains of different defect concentrations or species. Integrated spectral TRPL decay signal at 300 K for the NBE emission of the LPE GaN (***K***) is shown in Fig. 7(d). The obtained τ_{PL}^{RT} was 35 ps, which is consistently intermediate between the two Na-flux GaN crystals (***J***). The τ_{PL}^{RT}

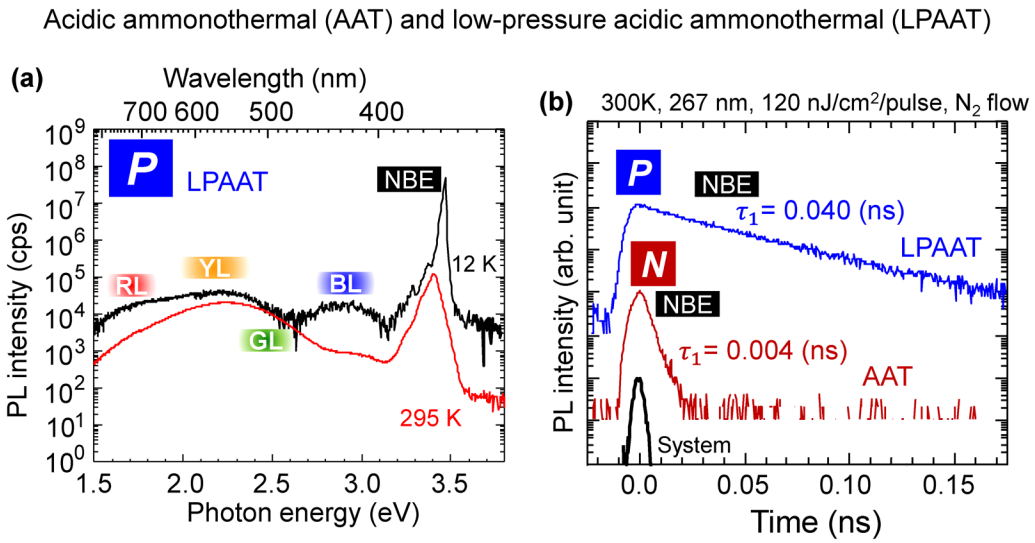

FIG. 8. (a) Steady-state PL spectra of the LPAAT GaN crystal (***P***).[61] Upper (black) and lower (red) curves show the spectra at 12 and 295 K, respectively. The PL intensity (*y*-) axis has a unit of cps and the spectra can be compared with those at different temperatures or other samples. The NBE emission includes free and bound excitons and their phonon replicas. (b) Integrated spectral TRPL decay signals measured at 300 K for the NBE emissions of the LPAAT GaN (***P***) (upper) and AAT GaN (***N***) (lower). The signal denoted by "System" shows the overall system response. The decay curves were fitted using a bi-exponential line shape function [Eq. (9)], and τ_1 values are denoted as representative τ_{PL}^{RT}. [The data in (a) are reproduced with permission from Kurimoto *et al.*, Appl. Phys. Express **15**, 055504 (2022). Copyright 2022 IOP Publishing LLC;[61] the data in (b) are reproduced with permission from Shima *et al.*, Appl. Phys. Lett. **124**, 181103 (2024). Copyright 2024 AIP Publishing LLC].[94]

value of 35 ps is plotted by the italic outline character ***K*** on a red square background at $N_{MGRC} = [C] = 3 \times 10^{17}\,cm^{-3}$ in Fig. 4, which is close to the red curve drawn for C_N.[29]

Steady-state PL spectra of the LPAAT GaN crystal (***P***) taken from the $(000\bar{1})$ growth plane are shown in Fig. 8(a).[61] At 12 K, the NBE peak intensity was more than three orders of magnitude higher than those of BL, YL, and RL bands. The BL band was also found in AAT and BAT crystals, which may originate from the complexes comprising hydrogenated V_{Ga} and O_N (H_{Ga}–O_N)[92] and/or $V_{Ga}O_N$ (V_{Ga}–O_N),[93] according to the fact that BAT and AAT crystals grown using supercritical NH_3 tend to contain high concentration H and O due to the difficulty in evacuating the autoclave and to the use of hygroscopic mineralizers.[61,94] The BL band seen in Fig. 8(a) is named "supercritical blue."[94] At 295 K, the GL band appears to be superimposed in the high energy side of the YL band. However, the NBE emission remained dominant and included at least two low-energy shoulders originating from LO phonon replicas. Integrated spectral TRPL decay signals measured at 300 K for the NBE emissions of the LPAAT GaN (***P***) and AAT GaN (***N***) are shown in Fig. 8(b).[94] Obviously, τ_{PL}^{RT} of LPAAT GaN (***P***) (40 ps) was an order of magnitude longer than that of AAT GaN (***N***) (4 ps). The results shown in Figs. 8(a) and 8(b) indicate far lower N_{MGRC} in the LPAAT GaN (***P***)[61,94] than that in the AAT GaN (***N***),[60] although the latter has been grown at higher pressure ($P_g > 200$ MPa) because an order of magnitude longer τ_{PL}^{RT} (Ref. 94) is a fingerprint of lower concentration of NMGRCs (N_{MGRC}). Evidence to support this assignment is that the room-temperature PL spectrum of the AAT GaN crystal was dominated by the YL band[60] although much higher excitation power density of 51 W cm^{-2} was used:[60] The result indicates higher concentration of DRCs (N_{DRC}). We note that τ_{PL}^{RT} of 40 ps for the LPAAT GaN (***P***) (Ref. 94) is the longest among AT GaN crystals: the BAT GaN crystal (***L***) exhibited short τ_{PL}^{RT} of approximately 4 ps (data not displayed). Because C_p of H_{Ga}, $V_{Ga}(O_N)_{3-4}$,[60] and $V_{Ga}(V_N)_n$ buried by H and/or O (Ref. 94) are approximately $3–8 \times 10^{-7}\,cm^3s^{-1}$ but the values are under confirmation,[94] τ_{PL}^{RT} for LPAAT (***P***) and AAT (***N***) GaN are not plotted in Fig. 4. Nevertheless, LPAAT method has advantages in fabricating plenty of large-size mosaic-free GaN wafers of better qualities than conventional AAT in a single run.[61]

B. p-type GaN

For obtaining a complete view of the recombination dynamics governed by MGRCs in GaN, those in p-type material must be understood. To comply with such demand, our state-of-the-art understandings on the origins and roles of MGRCs in Mg-doped p-GaN (GaN:Mg) epilayers and Mg-I/I p-GaN films are described in the following. Measured (S, W) for GaN:Mg epilayers grown by MOVPE (supplier ***Q***)[42] are shown by closed blue triangles in Fig. 9, for which annealing temperatures (T_a) are labeled. The calculated[41,60,73] (S, W) shown in Fig. 2 are plotted by open symbols for the determination of the defect species. The experimental (S_{DF}, W_{DF}) is plotted by closed black circle labeled DF-CTRL. Because the slope of an approximated line for the blue (S, W) plots nearly agreed[42] with the slope of a line connecting the calculated (S_{DF}, W_{DF}) and ($S_{V_{Ga}(V_N)_2}$, $W_{V_{Ga}(V_N)_2}$), major vacancy-type defects were identified as $V_{Ga}(V_N)_2$ (Ref. 42). Different from the seeded-grown epilayers,[26,42] defect species of Mg-I/I GaN varied

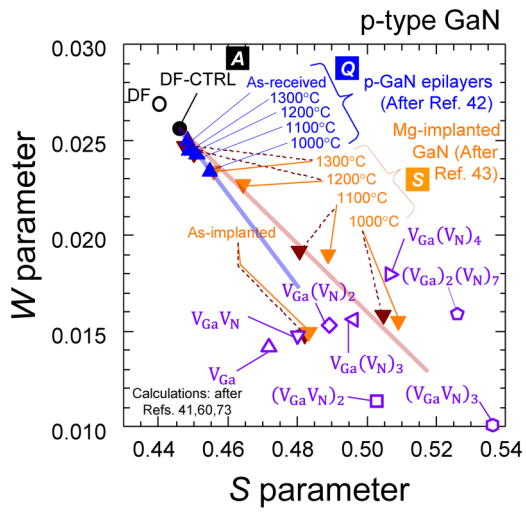

FIG. 9. Measured (S, W) for p-GaN supplied by ***Q*** (closed blue triangles)[42] and ***S*** (closed orange and carmine downward triangles).[43] For the plot ***Q***, annealing temperatures (T_a) are labeled. For ***S***, closed orange plots were measured with the 325.0 nm laser illumination and closed carmine plots were measured without illumination. Error bars are not given on all S–E plots because the experimental errors for the determination of both S and W were less than 0.1%. The calculated[41,60,73] (S, W) coordinates shown in Fig. 2 are plotted by open symbols to determine the vacancy defect species. The "experimental" (S_{DF}, W_{DF}) is plotted by closed black circle (DF-CTRL). [Calculated data plots are reproduced with permission from Ishibashi and Uedono, J. Phys. Conf. Ser. **505**, 012010 (2014). Copyright 2014 IOP Publishing LLC;[41] Uedono *et al.*, J. Cryst. Growth **448**, 117 (2016). Copyright 2016 Elsevier B.V.;[60] and Uedono *et al.*, Phys. Status Solidi B **255**, 1700521 (2018). Copyright 2017 WILEY-VCH Verlag GmbH & Co.;[73] Experimental data plots are reproduced with permission from Uedono *et al.*, Phys. Status Solidi B **252**, 2794 (2015). Copyright 2015 WILEY-VCH Verlag GmbH & Co.[42] and Uedono *et al.*, Phys. Status Solidi B **256**, 1900104 (2019).[43]].

with annealing conditions.[43,44,62] Common to three suppliers ***S***, ***T***, and ***U***, (S, W) plots almost overlapped with ($S_{V_{Ga}V_N}$, $W_{V_{Ga}V_N}$) coordinate right after I/I, as shown in Fig. 9, indicating the formation of high concentration $V_{Ga}V_N$ by Mg-I/I.[43,44,62] We note that closed orange plots were measured with the 325.0 nm laser illumination and closed carmine plots were measured without illumination. Here, the laser illumination was carried out to supply electrons in the vacancy-type defects to increase the sensitivity of the PAS measurement.[43,44,62] With increasing T_a, (S, W) of the Mg-I/I GaN (***S***) shifted once to the right and then to the upper left, indicating an agglomeration of $V_{Ga}V_N$ into large-size vacancy clusters. Because the slope of the approximated line for the downward triangle plots agreed with that of the line connecting the calculated (S_{DF}, W_{DF}) and ($S_{(V_{Ga}V_N)_3}$, $W_{(V_{Ga}V_N)_3}$), major vacancy-type defects after PIAs were assigned as $(V_{Ga}V_N)_3$ "hexavacancies."[43,44,62] We note that such movement of (S, W) was also found in ***T*** and ***U*** (Refs. 62 and 44, respectively). In case of supplier ***T***, (S, W) further shifted to the left,[62] approaching to a virtual line connecting calculated (S_{DF}, W_{DF}) and ($S_{(V_{Ga}V_N)_2}$, $W_{(V_{Ga}V_N)_2}$), because sequentially implanted excess N atoms may have buried some V_N to reduce the vacancy cluster size.[62]

In Fig. 9, (S, W) plots for suppliers ***T*** and ***U*** are not displayed to avoid congestion of data plots and approximated lines.

$\tau_{PL}^{RT} - N_{MGRC}$ relationships for the MGRCs in p-GaN are shown in Fig. 4: blue and orange curves show τ_{PL}^{RT} as a function of $V_{Ga}(V_N)_2$ and $(V_{Ga}V_N)_3$ concentrations, $[V_{Ga}(V_N)_2]$ and $[(V_{Ga}V_N)_3]$, respectively. They are drawn using Eqs. (3) and (5), where common $\tau_R = 40$ ns (Refs. 22 and 23) and $C_n = 5 \times 10^{-6}$ cm^3 s^{-1} (Refs. 26 and 27) are used. This C_n value is approximately an order of magnitude larger than C_p of $V_{Ga}V_N$ (6×10^{-7} cm^3 s^{-1}).[25] By using $v_{th} = v_n = 2.6 \times 10^7$ cm s^{-1} that is estimated from electron effective mass (m_n) of $0.20m_0$, corresponding σ_n is 2×10^{-13} cm^2, which is more than twice the σ_p of $V_{Ga}V_N$ in n-GaN (7×10^{-14} cm^2). These values are summarized in Table III. In Fig. 4, measured τ_{PL}^{RT} of the p-GaN epilayer (supplier ***R***) and Mg-I/I p-GaN (supplier ***S***) are plotted by italic outline characters on blue- and orange-square backgrounds, respectively. As clearly seen, τ_{PL}^{RT} of p-GaN is generally an order of magnitude shorter than the n-GaN for the same N_{MGRC} because of approximately three times larger σ_n and three times faster v_n.

Representative PL spectra of MOVPE GaN:Mg epitaxial film annealed at 850 °C (reference control sample), Ga- and N-polar 710-nm-deep I/I-GaN:Mg + H annealed at 1230 °C, and Ga- and N-polar 100-nm-deep I/I-GaN:Mg + H annealed at 1230 °C are shown in Figs. 10(a)–10(e), respectively.[27] All samples were provided by supplier ***S***, where [Mg] was commonly 1×10^{19} cm^{-3}. In Figs. 10(f)–10(j), PL spectra of as-implanted and annealed N-polar 100-nm-deep I/I-GaN:Mg + H of T_a = 800, 1000, 1100, and 1260 °C are shown, respectively. In each panel, PL spectra measured at 10 and 300 K are shown at the top and bottom, respectively. As shown in Fig. 10(a), the PL spectrum at 10 K of the Ga-polar GaN:Mg epilayer after annealing was dominated by the UVL band.[86,87,92,95,96] Also, a distinct peak due to the recombination of excitons bound to a neutral acceptor (acceptor-bound excitons: ABEs)[96] was observed. Both results indicate a progressive formation of Mg_{Ga} acceptors. In addition, the emergence of a BL band (magnesium blue)[91,95] at around 2.8 eV at 300 K [lower solid curve in Fig. 10(a)] is a fingerprint of p-type conductivity of GaN:Mg. The emissions from DRCs such as GL or RL were almost absent.

The Ga- and N-polar 710-nm-deep I/I-GaN:Mg + H also exhibited the UVL band at 10 K, as shown in Figs. 10(b) and 10(c), respectively, implying the formation of Mg_{Ga} acceptors.[86,91,93,96] However, their intensities were three orders of magnitude lower than the epilayer [Fig. 10(a)]. Moreover, distinct GL band[87] peculiar to I/I-GaN:Mg + H (Ref. 97) was dominant, and the RL band with almost equal intensity as UVL was found in both Figs. 10(b) and 10(c). These results indicate higher N_{MGRC} in I/I-GaN:Mg + H than the epilayer. Conversely, the Ga- and N-polar 100-nm-deep I/I-GaN:Mg + H exhibited a predominant UVL band at 10 K, of which intensities were approximately one and two orders of magnitude higher than the 710-nm-deep ones, as shown in Figs. 10(d) and 10(e), respectively. Moreover, a distinct ABE peak was found only in the 100-nm-deep samples, indicating lower N_{MGRC}. Indeed, both GL and RL were significantly suppressed. Therefore, the depth of I/I, i.e., total doses and energies used, seriously affected PL intensities:[97] to form constant [Mg] and [H] profiles, higher total doses and a greater number of times of I/I with higher energies are required for deeper profile samples, meaning that the samples suffer from severer I/I damage.[97]

TABLE III. Origins and capturing performances of major MGRCs in GaN at 300 K (v_{th}: $v_p = 9.1 \times 10^6$ cm s^{-1} and $v_n = 2.6 \times 10^7$ cm s^{-1}).

Conductivity type	Origin	Capturing performance for minority carriers: Capture coefficient ($cm^3 \cdot s^{-1}$)	Capturing performance for minority carriers: Capture cross section (cm^2)	General information and comments
n	$Fe_{Ga}^{3+/2+}$	$C_p = 5 \times 10^{-8}$ [a]	$\sigma_p = 6 \times 10^{-15}$ [a]	Residual impurity : transition metal: (E3)[b]
	$Mg_{Ga}^{0/-}$	$C_p = 1 \times 10^{-6}$	$\sigma_p = 1 \times 10^{-13}$	Residual impurity
	$C_N^{0/-}$	$C_p = 2 \times 10^{-7}$ [c]	$\sigma_p = 2 \times 10^{-14}$ [c]	DRC: indelible impurity for MOVPE (H1)[d]
	$V_{Ga}V_N$ [e]	$C_p = 6 \times 10^{-7}$ [e]	$\sigma_p = 7 \times 10^{-14}$ [e]	Major NRCs in n-GaN grown by HVPE, MOVPE, and MBE
	$V_{Ga}(V_N)_3$ [f]	…	…	NRC present in Na-flux crystals[f]
	$H_{V_{Ga}V_N}$ or $V_{Ga}(O_N)_4$ [g]	$C_p = 3–8 \times 10^{-7}$ [g]	$\sigma_p = 3–9 \times 10^{-14}$ [g]	DRC/NRC present in AAT and LPAAT crystals[g]
p	$V_{Ga}(V_N)_2$ [h]	$C_n = 5 \times 10^{-6}$ [i]	$\sigma_n = 2 \times 10^{-13}$ [i]	NRCs in MOVPE GaN:Mg epilayers[h,i]
	$(V_{Ga}V_N)_3$ [j]	$C_n = 5 \times 10^{-6}$ [k]	$\sigma_n = 2 \times 10^{-13}$ [k]	NRCs in Mg ion implanted (I/I) GaN after PIA[j,k]
DRCs	Mg_{Ga} (not so deep)	Probably same as	$Mg_{Ga}^{0/-}$ center	UVL (ultraviolet luminescence)[l]
	$Mg_{Ga} - V_N$	…	…	BL (magnesium blue)[m]
	$C_N^{+/0}$ (or C_{Ga})	…	…	BL (carbon blue)[n]
	$V_{Ga}(V_N)_n$ buried by H and/or O[o]	$C_p = 3–8 \times 10^{-7}$ [o]	$\sigma_p = 3–9 \times 10^{-14}$ [o]	BL (supercritical blue)[p]
	V_N-related	…	…	GL (green luminescence)[q]
	$C_N^{0/-}$	$C_p = 4 \times 10^{-7}$ [r]	$\sigma_p = 4 \times 10^{-14}$ [r]	YL (yellow luminescence)[s]
	$V_{Ga}O_N$	…	…	YL (yellow luminescence)
	V_N-related	…	…	RL (red luminescence)[p]

[a]Ref. 30.
[b]Ref. 82.
[c]Ref. 29.
[d]Ref. 54.
[e]Ref. 25.
[f]Ref. 57.
[g]Refs. 60 and 94.
[h]Ref. 42.
[i]Ref. 26.
[j]Refs. 43, 44, and 62.
[k]Refs. 27 and 28.
[l]Refs. 86, 87, 91, 95, and 96.
[m]Refs. 91 and 95.
[n]Refs. 32 and 85.
[o]Ref. 94.
[p]Refs. 92 and 93
[q]Ref. 87.
[r]Ref. 32.
[s]Refs. 45–47, 51, and 86.

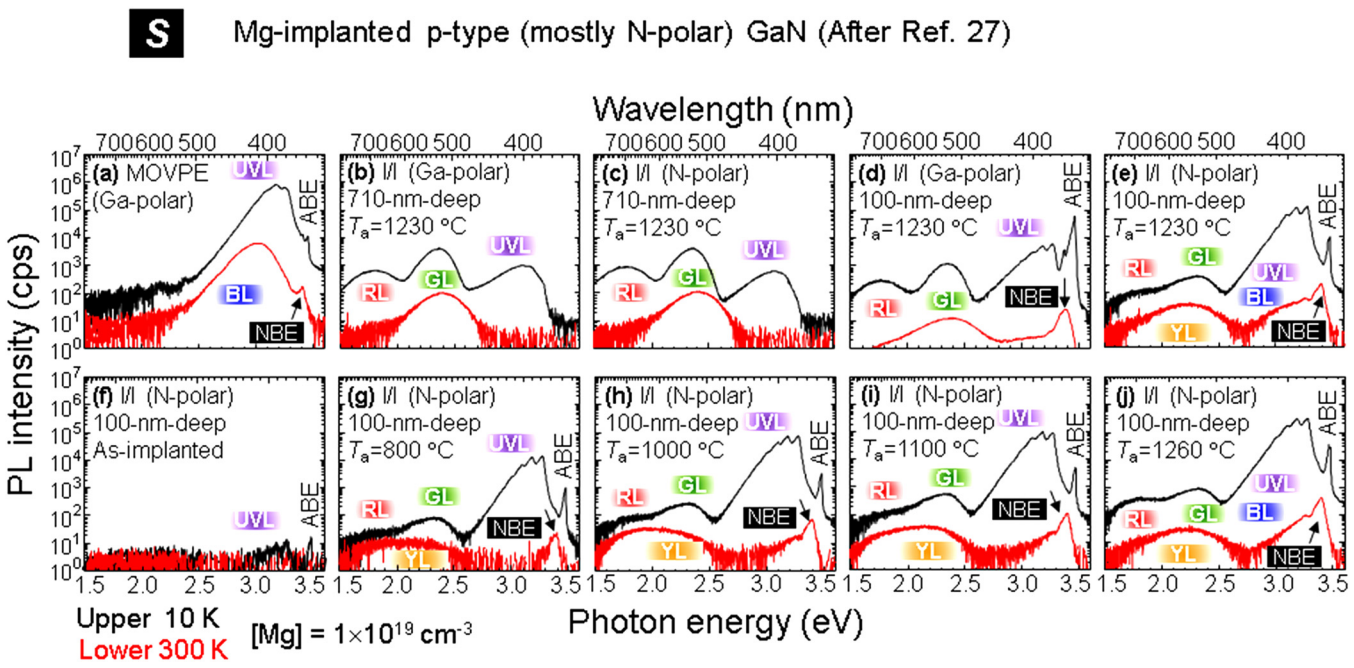

FIG. 10. Steady-state PL spectra at 10 K (top traces) and 300 K (bottom traces) of (a) Ga-polar GaN:Mg epilayer after annealing at 850 °C for 5 min in a N_2 ambient, (b) Ga-polar 710-nm-deep and (c) N-polar 710-nm-deep, (d) Ga-polar 100-nm-deep and (e) N-polar 100-nm-deep I/I-GaN:Mg + H annealed at T_a = 1230 °C. (f)–(j) PL spectra of N-polar I/I-GaN:Mg + H. The T_a values were (g) 800, (h) 1000, (i) 1100, and (j) 1260 °C. The [Mg] values were (a) 1.5×10^{19} and (b)–(j) 1.0×10^{19} cm^{-3}. All samples were fabricated on FS-GaN substrates by supplier ***S***. The PL intensity (*y*-) axis has a unit of cps, and all spectra can be quantitatively compared. [Reproduced with permission from Shima *et al.*, Appl. Phys. Lett. **113**, 191901 (2018). Copyright 2018 AIP Publishing LLC.][27]

At 300 K, the dominant PL peak of the control GaN:Mg epilayer was the BL band[91,96] often called Mg-blue, as shown in Fig. 10(a). The Ga- and N-polar 710-nm-deep I/I-GaN:Mg + H did not exhibit NBE emissions at 300 K, as shown in Figs. 10(b) and 10(c). The 100-nm-deep I/I samples, conversely, exhibited the NBE emissions at 300 K, as shown in Figs. 10(d) and 10(e). These results also support lower N_{MGRC}, more precisely N_{NRC}, in the 100-nm-deep samples. In addition to the NBE emission, the N-polar 100-nm-deep I/I-GaN:Mg + H exhibited distinct BL band (most likely Mg-blue)[91,93] as the low energy tail of UVL at 300 K, as shown in Fig. 10(e). Because the NBE emission intensity at 300 K of the N-polar 100-nm-deep I/I-GaN:Mg + H [Fig. 10(e)] was an order of magnitude higher than that of the Ga-polar edition [Fig. 10(d)], N_{NRC} in the N-polar sample is likely lower than the Ga-polar one, provided that the major NRCs in both samples have a common origin. Indeed, Mg-I/I GaN contained the same vacancy-type defects right after room-temperature I/I, namely, $V_{Ga}V_N$,[43,44,62] in the samples provided by supplier ***S***, ***T***, and ***U*** irrespective of polar directions.[43] Here, we mention that major NRCs and their concentrations in the Ga- and N-polar samples before I/I were also commonly $V_{Ga}V_N$ (Refs. 24 and 25) but lower than the dynamic range of the PAS measurement ($\sim 10^{15}$ cm^{-3}).[37] After the PIA, $V_{Ga}V_N$ commonly agglomerated into $(V_{Ga}V_N)_3$ (suppliers ***S*** and ***U***) except for the case of using sequential I/I of N (supplier ***T***), in which smaller vacancy clusters such as $(V_{Ga}V_N)_2$ were dominant.[62] Nevertheless, in addition to the depth of I/I, the crystallographic plane used for I/I and PIA is shown to be the other considerable factor affecting the PL intensities. As mentioned by Narita *et al.*,[98] the $(000\bar{1})$ plane offers better thermal stability than (0001) plane does, and therefore, the formation of vacancy clusters acting as NRCs at the surface during PIA is less likely. These considerations are consistent with the fact that the N-polar 100-nm-deep I/I-GaN:Mg + H showed a p-type conductivity.[97,98]

Sakurai *et al.*[64] showed that sequential I/I of Mg and N (I/I-GaN:Mg + N) into (0001) Ga-polar GaN followed by uncapped PIA in 1 GPa N_2 atmosphere at 1480 °C (supplier ***U***) gave rise to the observation of an intense UVL band originating from Mg_{Ga} acceptors[86,87,91,95,96] and suppressed GL band in the low-temperature cathodoluminescence (CL) spectra. Their results implied reduced $[V_N]$ by sequential I/I of N followed by the high-temperature UHPA. Recently, Uedono *et al.*[44] identified $(V_{Ga}V_N)_3$ as the major vacancy-type defects in the I/I-GaN:Mg + N after the UHPA at 1480 °C (supplier ***U***) and found progressive decrease in $[(V_{Ga}V_N)_3]$ by increasing T_a.[44] However, τ_{PL}^{RT} was shorter than the temporal resolution of our TRPL system[99] due to the presence of certain damaged zones at and near the surface[44,99] likely created by thermal stress.

Recently, Hu *et al.*[100] and Maeda *et al.*[101] independently reported the SRH lifetime (τ_{SRH}), which is expressed by $\tau_{SRH} = \sqrt{\tau_n \tau_p}$, where τ_n and τ_p are the lifetimes of an electron and

a hole at the recombination plane in the depletion layer, respectively, in p^+n^- and n^+p^- junctions of GaN as 12 ns (Ref. 100) and 46 ps (Ref. 101), respectively. This difference most likely reflects the differences in $\nu_{minority}$ and $\sigma_{minority}$ of the dominating NRCs. The results by Hu *et al.*[100] and Maeda *et al.*[101] are consistent with the authors' results.[25–28]

IV. SUMMARY

In this article, current knowledges on the origins and capture coefficients for minority carriers, $C_{minority}$, of major MGRCs in the state-of-the-art GaN substrates, epilayers, and Mg-implanted layers obtained using temporally resolved photoluminescence and PAS measurements are summarized. For unintentionally doped and n-type GaN grown by HVPE and MOVPE, τ_{PL}^{RT} for the near-band-edge emission was limited by the concentration of $C_N^{0/-}$, which exhibit the YL band,[45–47,51,86] or $V_{Ga}V_N$ that acts as major nonradiative recombination centers (NRCs)[24,25] when [C] was higher or lower, respectively, than approximately $10^{16}\,cm^{-3}$. The major vacancy-type defects in Na-flux GaN was identified as $V_{Ga}(V_N)_3$ that is larger in size than $V_{Ga}V_N$ of n-GaN grown from the vapor phase. The major defects in ammonothermal GaN were vacancy complexes such as V_{Ga} buried by a hydrogen (H_{Ga}) and/or vacancy clusters buried by impurities such as $H_{V_{Ga}V_N}$ and $V_{Ga}(O_N)_{3-4}$. All these vacancy complexes appear to act as MGRCs. For Mg-doped p-GaN epilayers, τ_{PL}^{RT} was limited by the concentration of $V_{Ga}(V_N)_2$. For Mg-implanted GaN, $V_{Ga}V_N$ and $(V_{Ga}V_N)_3$ are the major NRCs right after the implantation and after appropriate activation annealing, respectively. The origins and $C_{minority}$ values of major MGRCs in GaN at 300 K are summarized in Table III. Because of larger electron capture cross sections of $V_{Ga}(V_N)_2$ and $(V_{Ga}V_N)_3$ defects in addition to faster thermal velocity of electrons, τ_{PL}^{RT} of p-GaN is generally an order of magnitude shorter than that of n-GaN with the same N_{MGRC}. For the case of substitutional impurities in Si, a standardization of B, P, and low-level C concentrations well below the detection limits of analytical methods like SIMS measurements has been realized by using a low-temperature PL measurement.[83,84] As one of the perspectives, we propose a standardization of $\tau_{PL}^{RT} - N_{MGRC}$ curves in Fig. 4 as calibrating measures for quantifying (or semi-quantifying) the concentrations of respective MGRCs well below the detection limits of PAS and SIMS, as described in Sec. III A 1. We should again mention that the restriction for this proposal is the use of the weak-excitation conditions[22,24–28] that give rise to the excited minority carrier concentration constant and far below the concentrations of majority carriers and threshold for maintaining negligible classical[17,18] and trap-assisted[19] Auger–Meitner nonradiative recombination processes.

ACKNOWLEDGMENTS

This work was supported in part by MEXT-Program for Research and Development of Next-Generation Semiconductor to Realize Energy-Saving Society (No. JPJ005357), MEXT-Program for Creation of Innovative Core Technology for Power Electronics (No. JPJ009777), MEXT-Program of Dynamic Alliance for Open Innovation Bridging Human, Environment and Materials, and JSPS KAKENHI (Nos. JP16H06427 and JP21H01826) by MEXT and the Council for Science, Technology, and Innovation (CSTI), Cross-ministerial Strategic Innovation Promotion Program (SIP), "Next-generation power electronics-Research and Development of Fundamental Technologies for GaN Vertical Power Devices" (funding agency: NEDO).

AUTHOR DECLARATIONS

Conflict of Interest

The authors have no conflicts to disclose.

Author Contributions

Shigefusa F. Chichibu: Conceptualization (lead); Data curation (equal); Formal analysis (equal); Funding acquisition (equal); Investigation (lead); Methodology (lead); Project administration (equal); Resources (equal); Software (equal); Supervision (lead); Validation (lead); Visualization (lead); Writing – original draft (lead); Writing – review & editing (lead). **Kohei Shima:** Data curation (equal); Formal analysis (equal); Investigation (equal); Resources (equal); Software (equal); Validation (equal). **Akira Uedono:** Data curation (equal); Formal analysis (equal); Investigation (equal); Resources (equal); Validation (equal); Visualization (equal). **Shoji Ishibashi:** Data curation (equal); Formal analysis (equal); Investigation (equal); Methodology (equal); Software (equal); Supervision (equal). **Hiroko Iguchi:** Data curation (equal); Resources (equal). **Tetsuo Narita:** Data curation (equal); Investigation (equal); Resources (equal). **Keita Kataoka:** Data curation (equal); Formal analysis (equal); Investigation (equal). **Ryo Tanaka:** Data curation (equal); Formal analysis (equal); Resources (equal). **Shinya Takashima:** Data curation (equal); Formal analysis (equal); Funding acquisition (supporting); Investigation (equal). **Katsunori Ueno:** Data curation (equal); Formal analysis (equal); Funding acquisition (supporting); Investigation (equal). **Masaharu Edo:** Data curation (equal); Funding acquisition (supporting); Investigation (equal); Resources (equal). **Hirotaka Watanabe:** Data curation (equal); Investigation (equal); Resources (equal). **Atsushi Tanaka:** Data curation (equal); Investigation (equal); Resources (equal). **Yoshio Honda:** Data curation (equal); Formal analysis (supporting); Funding acquisition (supporting); Investigation (supporting); Project administration (supporting); Resources (equal); Supervision (supporting). **Jun Suda:** Funding acquisition (equal); Investigation (equal); Project administration (equal); Resources (equal). **Hiroshi Amano:** Funding acquisition (lead); Project administration (equal); Resources (equal); Software (equal). **Tetsu Kachi:** Data curation (equal); Investigation (equal); Resources (equal); Supervision (equal). **Toshihide Nabatame:** Data curation (equal); Funding acquisition (equal); Project administration (lead); Resources (equal); Validation (equal). **Yoshihiro Irokawa:** Data curation (equal); Investigation (equal); Resources (equal). **Yasuo Koide:** Data curation (equal); Formal analysis (equal); Funding acquisition (lead); Investigation (lead); Project administration (equal); Resources (equal); Visualization (equal).

DATA AVAILABILITY

The data that support the findings of this study are available in Refs. 44, 62, 63, and 73 in addition to this article.

REFERENCES

[1]S. J. Pearton, J. C. Zolper, R. J. Shul, and F. Ren, J. Appl. Phys. **86**, 1 (1999).
[2]In the statement of Scientific Background on the Nobel Prize in Physics 2014, Efficient blue light-emitting diodes leading to bright and energy-saving white light sources. Compiled by the Class for Physics of the Royal Swedish Academy of Sciences, October 7, 2014; I. Akasaki, Rev. Mod. Phys. **87**, 1119 (2015); H. Amano, *ibid* **87**, 1133 (2015); S. Nakamura, *ibid* **87**, 1139 (2015); *Introduction to Nitride Semiconductor Blue Lasers and Light Emitting Diodes*, edited by S. Nakamura and S. F. Chichibu (Taylor & Francis, London, 2000).
[3]S. Nakamura, M. Senoh, N. Iwasa, and S. Nagahama, Jpn. J. Appl. Phys. **34**, L797 (1995).
[4]S. Chichibu, T. Azuhata, T. Sota, and S. Nakamura, Appl. Phys. Lett. **69**, 4188 (1996).
[5]Y. Narukawa, Y. Kawakami, S. Fujita, S. Fujita, and S. Nakamura, Phys. Rev. B **55**, R1938 (1997).
[6]S. F. Chichibu, A. Uedono, T. Onuma, B. A. Haskell, A. Chakraborty, T. Koyama, P. T. Fini, S. Keller, S. P. DenBaars, J. S. Speck, U. K. Mishra, S. Nakamura, S. Yamaguchi, S. Kamiyama, H. Amano, I. Akasaki, J. Han, and T. Sota, Nat. Mater. **5**, 810 (2006); Philos. Mag. **87**, 2019 (2007); precisely reviewed in S. F. Chichibu, ECS J. Solid State Sci. Technol. **9**, 015016 (2020).
[7]Y. Saitoh, K. Sumiyoshi, M. Okada, T. Horii, T. Miyazaki, H. Shiomi, M. Ueno, K. Katayama, M. Kiyama, and T. Nakamura, Appl. Phys. Express **3**, 081001 (2010).
[8]J. Kolník, İ. H. Oğuzman, K. F. Brennan, R. Wang, P. P. Ruden, and Y. Wang, J. Appl. Phys. **78**, 1033 (1995).
[9]D. Shibata, R. Kajitani, M. Ogawa, K. Tanaka, S. Tamura, T. Hatsuda, M. Ishida, and T. Ueda, *IEDM Technical Digest* (IEEE, 2016), p. 248.
[10]M. Kodama, M. Sugimoto, E. Hayashi, N. Soejima, O. Ishiguro, M. Kanechika, K. Itoh, H. Ueda, T. Uesugi, and T. Kachi, Appl. Phys. Express **1**, 021104 (2008).
[11]T. Oka, T. Ina, Y. Ueno, and J. Nishii, Appl. Phys. Express **8**, 054101 (2015).
[12]Reviewed in H. Amano, Y. Baines, E. Beam, M. Borga, T. Bouchet, P. R. Chalker, M. Charles, K. J. Chen, N. Chowdhury, R. Chu *et al.*, J. Phys. D: Appl. Phys. **51**, 163001 (2018).
[13]T. Sugahara, H. Sato, M. Hao, Y. Naoi, S. Kurai, S. Tottori, K. Yamashita, K. Nishino, L. T. Romano, and S. Sakai, Jpn. J. Appl. Phys. **37**, L398 (1998).
[14]M. Auf der Maur, A. Pecchia, G. Penazzi, W. Rodrigues, and A. Di Carlo, Phys. Rev. Lett. **116**, 027401 (2016).
[15]S. F. Chichibu, H. Marchand, M. S. Minski, S. Keller, P. T. Fini, J. P. Ibbetson, S. B. Fleischer, J. S. Speck, J. E. Bowers, E. Hu, U. K. Mishra, S. P. DenBaars, T. Deguchi, T. Sota, and S. Nakamura, Appl. Phys. Lett. **74**, 1460 (1999); later precisely reviewed in S. F. Chichibu, ECS J. Solid State Sci. Technol. **9**, 015016 (2020).
[16]S. F. Chichibu, H. Miyake, and A. Uedono, Jpn. J. Appl. Phys. **61**, 050501 (2022).
[17]L. Meitner, Z. Phys. **9**, 131 (1922).
[18]P. Auger, C.R. Acad. Sci.(F) **177**, 169 (1923), see http://gallica.bnf.fr/ark:/12148/bpt6k3130n.image.f187.langFR
[19]F. Zhao, M. E. Turiansky, A. Alkauskas, and C. G. Van de Walle, Phys. Rev. Lett. **131**, 056402 (2023).
[20]W. Shockley and W. T. Read, Jr., Phys. Rev. **87**, 835 (1952).
[21]R. N. Hall, Phys. Rev. **87**, 387 (1952).
[22]S. F. Chichibu, K. Hazu, Y. Ishikawa, M. Tashiro, H. Namita, S. Nagao, K. Fujito, and A. Uedono, J. Appl. Phys. **111**, 103518 (2012).
[23]K. Kawakami, T. Nakano, and A. A. Yamaguchi, Proc. SPIE **9748**, 97480S (2016).
[24]S. F. Chichibu, A. Uedono, T. Onuma, T. Sota, B. A. Haskell, S. P. DenBaars, J. S. Speck, and S. Nakamura, Appl. Phys. Lett. **86**, 021914 (2005).
[25]S. F. Chichibu, A. Uedono, K. Kojima, H. Ikeda, K. Fujito, S. Takashima, M. Edo, K. Ueno, and S. Ishibashi, J. Appl. Phys. **123**, 161413 (2018).
[26]S. F. Chichibu, K. Shima, K. Kojima, S. Takashima, M. Edo, K. Ueno, S. Ishibashi, and A. Uedono, Appl. Phys. Lett. **112**, 211901 (2018).
[27]K. Shima, H. Iguchi, T. Narita, K. Kataoka, K. Kojima, A. Uedono, and S. F. Chichibu, App. Phys. Lett. **113**, 191901 (2018).
[28]S. F. Chichibu, K. Shima, K. Kojima, S. Takashima, K. Ueno, M. Edo, H. Iguchi, T. Narita, K. Kataoka, S. Ishibashi, and A. Uedono, Jpn. J. Appl. Phys. **58**, SC0802 (2019).
[29]K. Kojima, F. Horikiri, Y. Narita, T. Yoshida, H. Fujikura, and S. F. Chichibu, Appl. Phys. Express **13**, 012004 (2020).
[30]T. Aggerstam, A. Pinos, S. Marcinkevicius, M. Linnarsson, and S. Lourdudodd, J. Electron. Mater. **36**, 1621 (2007).
[31]T. Narita, Y. Tokuda, T. Kogiso, K. Tomita, and T. Kachi, J. Appl. Phys. **123**, 161405 (2018).
[32]Reviewed in M. A. Reshchikov, J. Appl. Phys. **129**, 121101 (2021).
[33]R. Krause-Rehberg and H. S. Leipner, *Positron Annihilation in Semiconductors, Solid-State Sciences* (Springer, Berlin, 1999), p. 127.
[34]P. G. Coleman, *Positron Beams and Their Application* (World Scientific, Singapore, 2000).
[35]K. Saarinen, T. Laine, S. Kuisma, J. Nissilä, P. Hautojärvi, L. Dobrzynski, J. M. Baranowski, K. Pakula, R. Stepniewski, M. Wojdak, A. Wysmolek, T. Suski, M. Leszczynski, I. Grzegory, and S. Porowski, Phys. Rev. Lett. **79**, 3030 (1997).
[36]A. Uedono, S. F. Chichibu, Z. Q. Chen, M. Sumiya, R. Suzuki, T. Ohdaira, T. Mikado, T. Mukai, and S. Nakamura, J. Appl. Phys. **90**, 181 (2001).
[37]F. Tuomisto and I. Makkonen, Rev. Mod. Phys. **85**, 1583 (2013).
[38]A. Uedono, S. Ishibashi, T. Ohdaira, and R. Suzuki, J. Cryst. Growth **311**, 3075 (2009).
[39]S. Ishibashi, Mater. Sci. Forum **445–446**, 401 (2004).
[40]S. Ishibashi, T. Tamura, S. Tanaka, M. Kohyama, and K. Terakura, Phys. Rev. B **76**, 153310 (2007).
[41]S. Ishibashi and A. Uedono, J. Phys.: Conf. Ser. **505**, 012010 (2014).
[42]A. Uedono, S. Takashima, M. Edo, K. Ueno, H. Matsuyama, H. Kudo, H. Naramoto, and S. Ishibashi, Phys. Status Solidi B **252**, 2794 (2015).
[43]A. Uedono, H. Iguchi, T. Narita, K. Kataoka, W. Egger, T. Koschine, C. Hugenschmidt, M. Dickmann, K. Shima, K. Kojima, S. F. Chichibu, and S. Ishibashi, Phys. Status Solidi B **256**, 1900104 (2019).
[44]A. Uedono, H. Sakurai, T. Narita, K. Sierakowski, M. Bockowski, J. Suda, S. Ishibashi, S. F. Chichibu, and T. Kachi, Sci. Rep. **10**, 17349 (2020).
[45]T. Ogino and M. Aoki, Jpn. J. Appl. Phys. **19**, 2395 (1980).
[46]J. Neugebauer and C. G. Van de Walle, Phys. Rev. B **50**, 8067 (1994);Appl. Phys. Lett. **69**, 503 (1996).
[47]J. L. Lyons, A. Janotti, and C. G. Van de Walle, Appl. Phys. Lett. **97**, 152108 (2010).
[48]A. Y. Polyakov, N. B. Smirnov, A. S. Usikov, A. V. Govorkov, and B. V. Pushniy, Solid-State Electron. **42**, 1959 (1998).
[49]V. A. Joshkin, C. A. Parker, S. M. Bedair, J. F. Muth, I. K. Shmagin, R. M. Kolbas, E. L. Piner, and R. J. Molnar, J. Appl. Phys. **86**, 281 (1999).
[50]A. F. Wright, J. Appl. Phys. **90**, 1164 (2001).
[51]C. G. Van de Walle and J. Neugebauer, J. Appl. Phys. **95**, 3851 (2004).
[52]G. Piao, K. Ikenaga, Y. Yano, H. Tokunaga, A. Mishima, Y. Ban, T. Tabuchi, and K. Matsumoto, J. Cryst. Growth **456**, 137 (2016).
[53]F. Horikiri, Y. Narita, T. Yoshida, T. Kitamura, H. Ohta, T. Nakamura, and T. Mishima, Jpn. J. Appl. Phys. **56**, 061001 (2017).
[54]T. Narita, K. Tomita, Y. Tokuda, T. Kogiso, M. Horita, and T. Kachi, J. Appl. Phys. **124**, 215701 (2018).
[55]A. Tanaka, Y. Ando, K. Nagamatsu, M. Deki, H. Cheong, B. Ousmane, M. Kushimoto, S. Nitta, Y. Honda, and H. Amano, Phys. Status Solidi A **215**, 1700645 (2018).
[56]H. Yamane, M. Shimada, S. J. Clarke, and F. J. DiSalvo, Chem. Mater. **9**, 413 (1997).
[57]A. Uedono, M. Imanishi, M. Imade, M. Yoshimura, S. Ishibashi, M. Sumiya, and Y. Mori, J. Cryst. Growth **475**, 261 (2017).
[58]T. Yamada, H. Yamane, H. Iwata, and S. Sarayama, J. Cryst. Growth **281**, 242 (2005).
[59]T. Onuma, T. Yamada, H. Yamane, and S. F. Chichibu, Appl. Phys. Express **2**, 091004 (2009).
[60]A. Uedono, Y. Tsukada, Y. Mikawa, T. Mochizuki, H. Fujisawa, H. Ikeda, K. Kurihara, K. Fujito, S. Terada, S. Ishibashi, and S. F. Chichibu, J. Cryst. Growth **448**, 117 (2016).

[61]D. Tomida, Q. Bao, M. Saito, R. Osanai, K. Shima, K. Kojima, T. Ishiguro, and S. F. Chichibu, Appl. Phys. Express **13**, 055505 (2020); K. Kurimoto, Q. Bao, Y. Mikawa, K. Shima, T. Ishiguro, and S. F. Chichibu, Appl. Phys. Express **15**, 055504 (2022).
[62]A. Uedono, R. Tanaka, S. Takashima, K. Ueno, M. Edo, K. Shima, K. Kojima, S. F. Chichibu, and S. Ishibashi, Sci. Rep. **11**, 20660 (2021).
[63]K. Shima, R. Tanaka, S. Takashima, K. Ueno, M. Edo, K. Kojima, A. Uedono, S. Ishibashi, and S. F. Chichibu, Appl. Phys. Lett. **119**, 182106 (2021).
[64]H. Sakurai, M. Omori, S. Yamada, Y. Furukawa, H. Suzuki, T. Narita, K. Kataoka, M. Horita, M. Bockowski, J. Suda, and T. Kachi, Appl. Phys. Lett. **115**, 142104 (2019).
[65]K. Sierakowski, R. Jakiela, B. Lucznik, P. Kwiatkowski, M. Iwinska, M. Turek, H. Sakurai, T. Kachi, and M. Bockowski, Electronics **9**, 1380 (2020).
[66]P. E. Blöchl, Phys. Rev. B **50**, 17953 (1994).
[67]G. Kresse and D. Joubert, Phys. Rev. B **59**, 1758 (1999).
[68]J. P. Perdew, K. Burke, and M. Ernzerhof, Phys. Rev. Lett. **77**, 3865 (1996).
[69]E. Boronski and R. M. Nieminen, Phys. Rev. B **34**, 3820 (1986).
[70]M. J. Puska, A. P. Seitsonen, and R. M. Nieminen, Phys. Rev. B **52**, 10947 (1995).
[71]S. F. Chichibu, A. Uedono, K. Kojima, K. Koike, M. Yano, S. Gonda, and S. Ishibashi, J. Appl. Phys. **127**, 215704 (2020).
[72]S. Ishibashi and A. Uedono, J. Phys.: Conf. Ser. **674**, 012020 (2016).
[73]A. Uedono, S. Takashima, M. Edo, K. Ueno, H. Matsuyama, W. Egger, T. Koschine, C. Hugenschmidt, M. Dickmann, K. Kojima, S. F. Chichibu, and S. Ishibashi, Phys. Status Solidi B **255**, 1700521 (2018).
[74]A. Van Veen, H. Schut, M. Clement, J. M. M. de Nijs, A. Kruseman, and M. R. Ijpma, Appl. Surf. Sci. **85**, 216 (1995).
[75]T. Onuma, Y. Kagamitani, K. Hazu, T. Ishiguro, T. Fukuda, and S. F. Chichibu, Rev. Sci. Instrum. **83**, 043905 (2012).
[76]P. Corfdir, P. Lefebvre, J. Levrat, A. Dussaigne, J.-D. Ganiere, D. Martin, J. Ristic, T. Zhu, N. Grandjean, and B. Deveaud-Pledran, J. Appl. Phys. **105**, 043102 (2009).
[77]P. Corfdir, J. Ristic, P. Lefebvre, T. Zhu, A. Dussaigne, J. D. Ganiere, N. Grandjean, and B. Deveaud-Pledran, Appl. Phys. Lett. **94**, 201115 (2009).
[78]M. Kagaya, P. Corfdir, J.-D. Ganiere, B. Deveaud-Pledran, N. Grandjean, and S. F. Chichibu, Jpn. J. Appl. Phys. **50**, 111002 (2011).
[79]Y. Ishikawa, M. Tashiro, K. Hazu, K. Furusawa, H. Namita, S. Nagao, K. Fujito, and S. F. Chichibu, Appl. Phys. Lett. **101**, 212106 (2012).
[80]K. Furusawa, Y. Ishikawa, M. Tashiro, K. Hazu, S. Nagao, H. Ikeda, K. Fujito, and S. F. Chichibu, Appl. Phys. Lett. **103**, 052108 (2013).
[81]F. Tuomisto, T. Kuittinen, M. Zając, R. Doradziński, and D. Wasik, J. Cryst. Growth **403**, 114 (2014).
[82]M. Horita, T. Narita, T. Kachi, and J. Suda, Appl. Phys. Express **13**, 071007 (2020).
[83]M. Tajima, Appl. Phys. Lett. **32**, 719 (1978).
[84]M. Tajima, S. Samata, S. Nakagawa, Y. Shinozuka, J. Oriyama, and N. Ishihara, Jpn. J. Appl. Phys. **60**, 026501 (2021).
[85]R. Armitage, Q. Yang, and E. R. Weber, J. Appl. Phys. **97**, 073524 (2005).
[86]M. A. Reshchikov and H. Morkoç, J. Appl. Phys. **97**, 061301 (2005).
[87]M. A. Reshchikov, D. O. Demchenko, J. D. McNamara, S. F. Garrido, and R. Calarco, Phys. Rev. B **90**, 035207 (2014).
[88]E. F. Schubert, I. D. Goepfert, W. Grieshaber, and J. M. Redwing, Appl. Phys. Lett. **71**, 921 (1997).
[89]M. Yoshikawa, M. Kunzer, J. Wagner, H. Obloh, P. Schlotter, R. Schmidt, N. Herres, and U. Kaufmann, J. Appl. Phys. **86**, 4400 (1999).
[90]B. J. Skromme, K. Palle, C. D. Poweleit, H. Yamane, M. Aoki, and F. J. DiSalvo, J. Cryst. Growth **246**, 299 (2002).
[91]G. Pozina, P. P. Paskov, J. P. Bergman, C. Hemmingsson, L. Hultman, B. Monemar, H. Amano, I. Akasaki, and A. Usui, Appl. Phys. Lett. **91**, 221901 (2007).
[92]M. Toth, K. Fleischer, and M. R. Phillips, Phys. Rev. B **59**, 1575 (1999).
[93]H. C. Yang, T. Y. Lin, and Y. F. Chen, Phys. Rev. B **62**, 12593 (2000).
[94]K. Shima, K. Kurimoto, Q. Bao, Y. Mikawa, M. Saito, D. Tomida, A. Uedono, S. Ishibashi, T. Ishiguro, and S. F. Chichibu, Appl. Phys. Lett. **124**, 181103 (2024).
[95]H. Alves, M. Bohm, A. Hofstaetter, H. Amano, S. Einfeldt, D. Hommel, D. M. Hofmann, and B. K. Meyer, Physica B **308–310**, 38 (2001).
[96]B. Monemar, P. P. Paskov, G. Pozina, C. Hemmingsson, J. P. Bergman, T. Kawashima, H. Amano, I. Akasaki, T. Paskova, S. Figge, D. Hommel, and A. Usui, Phys. Rev. Lett. **102**, 235501 (2009).
[97]K. Kataoka, T. Narita, H. Iguchi, T. Uesugi, and T. Kachi, Phys. Status Solidi B **255**, 1700379 (2018).
[98]T. Narita, T. Kachi, K. Kataoka, and T. Uesugi, Appl. Phys. Express **10**, 016501 (2017).
[99]K. Shima, H. Sakurai, S. Ishibashi, A. Uedono, M. Bockowski, J. Suda, T. Kachi, and S. F. Chichibu, presented at the 83rd Fall Meeting of Japan Society of Applied Physics (2022), No. 22p-B204-7.
[100]Z. Hu, K. Nomoto, B. Song, M. Zhu, M. Qi, M. Pan, X. Gao, V. Protasenko, D. Jena, and H. G. Xing, Appl. Phys. Lett. **107**, 243501 (2015).
[101]T. Maeda, T. Narita, H. Ueda, M. Kanechika, T. Uesugi, T. Kachi, T. Kimoto, M. Horita, and J. Suda, Jpn. J. Appl. Phys. **58**, SCCB14 (2019).